

TAEN: A Model-Constrained Tikhonov Autoencoder Network for Forward and Inverse Problems

Hai Van Nguyen^a, Tan Bui Thanh^{a,b}, Clint Dawson^{a,b}

^a*Department of Aerospace Engineering and Engineering Mechanics, the University of Texas at Austin, Austin, 78712, Texas, USA*

^b*The Oden Institute for Computational Engineering and Sciences, the University of Texas at Austin, Austin, 78712, Texas, USA*

Abstract

Efficient real-time solvers for forward and inverse problems are essential in engineering and science applications. Machine learning surrogate models have emerged as promising alternatives to traditional methods, offering substantially reduced computational time. Nevertheless, these models typically demand extensive training datasets to achieve robust generalization across diverse scenarios. While physics-based approaches can partially mitigate this data dependency and ensure physics-interpretable solutions, addressing scarce data regimes remains a challenge. Both purely data-driven and physics-based machine learning approaches demonstrate severe overfitting issues when trained with insufficient data. *We propose a novel model-constrained Tikhonov autoencoder neural network framework, called TAEN, capable of learning both forward and inverse surrogate models using a single arbitrary observational sample.* We develop comprehensive theoretical foundations including forward and inverse inference error bounds for the proposed approach for linear cases. For comparative analysis, we derive equivalent formulations for pure data-driven and model-constrained approach counterparts. At the heart of our approach is a data randomization strategy with theoretical justification, which functions as a generative mechanism for exploring the training data space, enabling effective training of both forward and inverse surrogate models even with a single observation, while regularizing the learning process. We validate our approach through extensive numerical experiments on two challenging inverse problems: 2D heat conductivity inversion and initial condition reconstruction for time-dependent 2D Navier–Stokes equations. Results demonstrate that TAEN achieves accuracy comparable to traditional Tikhonov solvers and numerical forward solvers for both inverse and forward problems, respectively, while delivering orders of magnitude computational speedups.

Keywords: Forward problem, Inverse problem, randomization, model-constrained autoencoder, deep learning, partial differential equations.

1. Introduction

Partial differential equations (PDEs) serve as the mathematical foundation for describing physical phenomena in science and engineering applications [81, 34]. Generally, these

equations lack analytical solutions except in limited special cases, necessitating numerical approaches such as finite difference [68, 29, 63], finite element [72, 74], and finite volume methods [23, 46]. These computational techniques, while essential, often impose significant computational burdens, particularly for high-dimensional problems. In this context, PDE-constrained inverse problems represent pervasive mathematical methods in inferring knowledge from experimental and observational data by leveraging numerical simulations and models [41, 67, 87, 83]. Among various methodologies, the Tikhonov regularization framework stands as a predominant approach for addressing general inverse problems [36, 96, 57, 31]. This optimization-based methodology necessitates multiple evaluations of the forward model, which is typically governed by PDEs. Consequently, PDE-constrained inverse problems face two primary challenges: they not only demand substantial computational resources but also require extensive processing time to obtain solutions, making them impractical for applications requiring real-time responses.

Machine learning has demonstrated remarkable success across diverse domains, from computer vision and natural language processing [43, 21, 85] to physics-based applications including experimental design [79, 15] and digital twins [56, 73, 4]. The autoencoder architecture has emerged as a versatile framework for applications in image processing tasks such as denoising and inpainting [14, 32, 35], as well as in transformer-based natural language processing systems [85]. In science and engineering applications, machine learning approaches have demonstrated significant potential in developing computationally efficient surrogate models for both forward and inverse problems [71, 64, 61, 84, 58, 49, 52]. Traditional data-driven learning methodologies, which construct surrogate models without incorporating physical principles [91, 3], face several limitations. These include the requirement for extensive training datasets to achieve accurate forward or inverse surrogate models [47, 53, 1, 65, 91], limited generalization capabilities, and generating non-physical solutions. To address these challenges, physics-based machine learning approaches have been developed, integrating governing physical principles into the learning framework [71, 62, 59, 24]. However, as noted in [59], these physics-based approaches remain susceptible to overfitting when training data are scarce. The acquisition of comprehensive training datasets presents significant challenges in many engineering applications due to prohibitive costs or practical limitations. For instance, in full wave-form inversion, data collection is constrained by the substantial expenses associated with sensor placement (such as multi-million dollar oil well drilling operations) or accessibility challenges in certain environments (like deep ocean floors). This underscores the critical need for developing machine learning methodologies capable of constructing physics-interpretable surrogate models from minimal training samples.

Physics-informed neural networks (PINNs) [71] employ neural networks to parametrize solutions for both PDEs [71, 89, 13] and PDE-constrained inverse problems [71, 37, 38, 17], using spatial or temporal variables as inputs. The neural network parameters are optimized through objective functions comprising multiple loss terms, including PDE constraints, boundary conditions, initial conditions, and observation data misfits. An alternative approach, aligned with the concept of neural fields [92], has emerged in inverse problem solving [82, 80, 24, 6]. This methodology processes neural network inverted solutions through

numerical forward simulations to generate synthetic data, which is then reconciled with observational data to optimize the neural representation of solutions. While these approaches offer the advantage of mesh-independent solutions—capable of producing results at any spatiotemporal point post-training—they suffer from a significant limitation: the requirement to retrain the network for each new scenario, including variations in model parameters, boundary conditions, or observation sets. As such, these methods do not have the ability to generalize to unseen inference cases, which are critical requirements for making physics-based machine learning surrogate models viable in real-time applications. Furthermore, research has shown that PINNs demand extensive training periods and numerous architectural experiments to achieve adequate solution convergence [20]. This limitation becomes particularly problematic in inverse problems, in which the PDE must be solved repeatedly throughout optimization iterations. Alternative approaches proposed in [76, 95] focus on learning regularizer functions for inverse problems from extensive training datasets. While these learned neural network regularizers enhance solution quality compared to traditional Tikhonov regularization, they essentially represent another computationally intensive method for solving PDEs or PDE-constrained inverse problems, making them unsuitable for real-time applications.

Various methodologies have emerged for learning parameter-to-observation maps, or more general, numerical PDE simulations, focusing on predicting solution for unseen scenarios from historical snapshots of solutions. Neural ODE [16] and related approaches [84, 90, 58, 97] propose learning the right-hand side of semi-discretized equations, offering the distinctive advantage of predicting solutions at arbitrary temporal points through time integration schemes. Alternative frameworks employ recurrent neural network architectures [44, 27, 55] or transformer-based models [28, 48] to process sequences of historical solution snapshots for future state predictions. These methods, however, are usually constrained by the requirement of uniform temporal sampling for both input and predicted solutions. Another promising direction involves learning dynamics in latent space, where solutions are projected into lower-dimensional representations using autoencoder-like architectures [93, 88, 33, 40, 45] or graph pooling techniques [5, 69]. In these approaches, neural networks are employed to approximate the evolution of the system in the compressed latent space. The operator learning approach [49, 52] potentially offers computationally efficient surrogate models by directly learning functional mappings between parameter fields and target solutions across the physical domain. While all these methodologies demonstrate considerable promise in capturing PDE system dynamics and generating future solution predictions, they generally require substantially large training data to develop accurate surrogate forward models or functional mapping operators.

A variety of machine learning approaches have been developed to create generalizable inverse solvers for PDE-constrained inverse problems. Several researchers [39, 59, 65] have introduced methods that directly regularize neural network inverse surrogate models through differentiable PDE solvers. In these approaches, the predicted Parameters of Interest (PoI) from neural networks are processed through PDE solvers to regenerate synthetic observation data, which is expected to match training observation input data. These physics-based methods demonstrate significant improvements over pure data-driven approaches

given equivalent training data volumes. However, the training data requirements for effective inverse mappings correlate with the non-linearity of the parameter-to-observables (PtO) map, making them inherently problem-specific. Our previous research [59] introduced the model-constrained TNet approach for learning Tikhonov inverse solvers from a finite training dataset. Notably, with identical sample sizes, both pure machine learning and physics-based approaches face overfitting challenges compared to TNet. Related work [51, 39] proposes first training the forward map to learn the PDE solver, which then constrains the inverse map learning process with pre-trained PDE surrogate models, thereby reducing overall training costs. Alternative approaches [18, 8] employ dual autoencoder architectures to compress both observation and PoI data spaces into lower-dimensional latent representations, followed by learning linear inverse mappings between these compressed spaces. Additionally, variational autoencoder architectures have been widely adopted for probabilistic inverse problem solving [30, 2]. Some efforts [30] focus on simultaneous learning of forward and inverse surrogate models. However, in this work, concurrent training of encoders and decoders for both forward and inverse mappings can complicate training convergence due to the increased dimensionality of the trainable parameter space, and the competition between the encoder and the decoder.

In scientific machine learning, enhancing surrogate model generalization remains a critical objective and a grand challenge. Several researchers [66, 94, 22, 77, 26] have proposed incorporating input-gradient information into the loss function to improve neural network solution accuracy and generalization capabilities. However, the computational cost of explicitly computing Jacobian matrices through back-propagation for optimization is substantial, particularly for high-dimensional input problems, due to the requirement for double back-propagation. While [61] demonstrates that exploiting low-rank properties of Jacobian matrices can reduce computational overhead, our previous work [58, 59] shows that comparable regularization effects can be achieved through data randomization techniques in forward surrogate model learning. This randomization approach, which introduces controlled noise to neural network input data, has been shown to enhance long-term predictive stability [78, 70, 58]. Theoretical foundations established in [75, 7, 54] demonstrate that input data perturbation effectively functions as Tikhonov regularization, promoting input-space smoothness in neural network responses. Our recent work [59, 58] show that randomization induces regularization on the derivatives without actually computing them (which we try to avoid due to the aforementioned reasons). Our works further validate that data randomization not only improves the generalization capability of learned inverse surrogate models to unseen observation scenarios but also substantially reduces training data requirements.

This paper extends our previous research [59] by introducing TAEN, a Tikhonov autoencoder model-constrained learning framework **capable of addressing both forward and inverse problems using only a single arbitrary observational sample**. For comparative analysis, we examine various autoencoder architectures, including pure data-driven approaches [91] and model-constrained methods [65, 24, 39]. Our theoretical analysis provides forward and inverse solution error estimates across all approaches for linear problems. These derivations, combined with numerical evidence, suggest that both pure data-driven and model-constrained approaches may yield suboptimal learning strategies for inverse prob-

lems due to potential training data bias. In contrast, **TAEN** employs data randomization techniques with just one arbitrary observational sample to learn Tikhonov inverse solutions. For linear inverse problems, the approach successfully recovers Tikhonov-regularized solutions while maintaining exact compliance with governing equations at training points. Furthermore, given the pre-trained inverse map encoder and the same observation sample, the decoder accurately represents the forward map/parameter to observable (PtO) mapping for linear problems. We also provide theoretical justification for sequential encoder-decoder training rather than simultaneous optimization. The effectiveness of our proposed approach is demonstrated through extensive numerical experiments on two challenging applications: 2D inverse heat conductivity inversion and initial condition reconstruction for time-dependent 2D Navier–Stokes equations.

There are several limitations to our approaches. The primary constraint stems from the requirement for a differentiable solver, which results in training and memory costs that scale with multiple forward solution computations. One potential solution, as demonstrated in [39], is to learn surrogate models for PDEs before incorporating them into **TAEN** framework. A second limitation arises from **TAEN**’s design principle: learn the Tikhonov inverse solver and the forward solver at the same time. While it offers improved interpretability and accuracy compared to purely data-driven approaches, its inverse performance is inherently bounded by the traditional Tikhonov method. Consequently, for scenarios with abundant data, alternative approaches such as [53, 1, 47] may achieve superior accuracy relative to traditional Tikhonov methods, though these alternatives cannot provide real-time inverse solutions as **TAEN** does. Finally, while **TAEN** offers an advantage over existing deep neural network approaches by deriving its regularization parameter directly from the Tikhonov framework—rather than lacking a principled parameter selection method—the challenge of determining optimal regularization parameters remains, just like any approach in finding optimal regularization parameter. This optimization task is highly problem-dependent and computationally extensive.

The paper’s organization is as follows. Section 2.1 establishes the fundamental framework of linear and nonlinear PDEs and PDE-constrained inverse problems, along with notational conventions. Section 2.2 examines data-driven autoencoder machine learning approaches, specifically **nPOP** and **nOPO**. Section 2.3 explores model-constrained autoencoder machine learning approaches—**mcPOP**, **mcOPO**, and **mcOPO-Full**—which learn inverse and forward mappings while incorporating model constraints from the parameter-to-observable map of the discretized PDE. In Section 2.4, we introduce Tikhonov autoencoder neural networks, **TAEN** and its variant **TAEN-Full**, designed to learn Tikhonov solver and PtO/forward maps while eliminating unnecessary training biases. Section 2.5 provides a detailed analysis comparing sequential versus simultaneous training strategies for encoder and decoder networks. Section 3 presents comprehensive numerical experiments validating our theoretical developments through applications to 2D inverse heat conductivity problems and inverse initial conditions for 2D time-dependent Navier-Stokes equations. The paper concludes in Section 4 with future research directions, while detailed proofs of theoretical results are provided in Section 5.

2. Methodology

2.1. Problem setting and notation

In this research, we explore various auto-encoder approaches for learning the following functions: the parameter-to-observable (PtO) map or forward map (transforming PoIs to PDE solutions), and inverse mappings (converting observables to PoIs). Our investigation encompasses naïve machine learning approaches (Section 2.2), model-constrained machine learning techniques (Section 2.3), and Tikhonov model-constrained machine learning strategies (Section 2.4). We deviate from traditional concurrent encoder-decoder training by implementing a sequential approach—first training the encoder network, then optimizing the decoder using the pre-trained encoder. The comparative merits of sequential versus simultaneous training are analyzed in Section 2.5. Our notation follows standard conventions: matrices are denoted by capital letters, vectors by boldface normal letters, and scalars by lowercase Roman letters. We seek to learn the forward map $\mathcal{G} : \mathbb{R}^n \mapsto \mathbb{R}^p$ governed by a PDE:

$$\boldsymbol{\omega} = \mathcal{G}(\mathbf{u}),$$

or its corresponding parameter-to-observable (PtO) map:

$$\mathbf{y} = B \circ \mathcal{G}(\mathbf{u}) + \boldsymbol{\eta} = B\boldsymbol{\omega} + \boldsymbol{\eta},$$

where $\boldsymbol{\eta}$ represents observation noise, $\mathbf{u} \in \mathbb{R}^n$ denotes the parameter of interest (PoI),¹ $\boldsymbol{\omega} \in \mathbb{R}^p$ represents the PDE solution, $B : \mathbb{R}^p \mapsto \mathbb{R}^m$ defines the observation operator, and $\mathbf{y} \in \mathbb{R}^m$ represents the observation. For inverse problems, we aim to learn the mapping:

$$\mathbf{u} = (B \circ \mathcal{G})^{-1}(\mathbf{y}).$$

Note that the inverse map is not well-defined in general. As we shall show, we learn regularized inverse maps instead.

For clarity in our derivations, we define the following notations: Training data matrices $U \in \mathbb{R}^{n \times n_t}$ and $Y \in \mathbb{R}^{m \times n_t}$ contain n_t PoI samples and n_t observation samples, respectively. For linear problems, G represents the linear forward map, while $G^B = B \circ G$ denotes its corresponding linear PtO map. Neural network components Ψ_e and Ψ_d represent encoder and decoder networks, respectively. In linear neural networks, $\{W_e, \mathbf{b}_e\}$ and $\{W_d, \mathbf{b}_d\}$ denote weight matrices and bias vectors for encoder and decoder networks, respectively. We define additional notations: $\bar{\mathbf{x}} = X \frac{\mathbf{1}}{n_t}$ computes the column mean of matrix X , $\tilde{X} = X - \bar{\mathbf{x}}\mathbf{1}^T$ represents the centered-column matrix, $\mathbf{1}$ denotes a column vector of ones, while $\|\cdot\|_F$ indicates the Frobenius norm and \dagger denotes matrix pseudo-inverse.

2.2. Naïve autoencoder learning approaches

In this section, we present two naïve data-driven autoencoder approaches that are commonly employed for learning PtO and inverse mappings in engineering applications. These approaches rely exclusively on training data pairs $\{U, Y\}$ without incorporating any physical models or domain knowledge into their loss functions [30, 18, 91, 3].

¹The parameter vector could be a discrete representation of some distributed parameter field.

2.2.1. Naïve autoencoder PtO-inverse learning approach **nPOP**

In this approach, we learn the encoder for PtO map and the decoder for inverse map. Given the training data set $\{U, Y\}$, the loss functions are defined as

$$\begin{aligned}\Psi_e^* &= \min_{\Psi_e} \frac{1}{2} \|\Psi_e(U) - Y\|_F^2, \\ \Psi_d^* &= \min_{\Psi_d} \frac{1}{2} \|\Psi_d(\Psi_e^*(U)) - U\|_F^2.\end{aligned}\tag{nPOP}$$

For analytical insights, we examine a noise-free linear inverse problem using linear neural networks. The linear encoder learns the PtO map as $Z = \Psi_e(U) = W_e U + \mathbf{b}_e \mathbf{1}^T$, while the linear decoder learns the inverse map $\Psi_d(Z) = W_d Z + \mathbf{b}_d \mathbf{1}^T$. Substituting into eq. (nPOP), we obtain the following

$$\begin{aligned}W_e^*, \mathbf{b}_e^* &= \min_{W_e, \mathbf{b}_e} \frac{1}{2} \|W_e U + \mathbf{b}_e \mathbf{1}^T - Y\|_F^2, \\ W_d^*, \mathbf{b}_d^* &= \min_{W_d, \mathbf{b}_d} \frac{1}{2} \|W_d (W_e^* U + \mathbf{b}_e^* \mathbf{1}^T) + \mathbf{b}_d \mathbf{1}^T - U\|_F^2.\end{aligned}\tag{1}$$

Applying the first-order optimality conditions for eq. (1) yields the following optimal solutions (see the complete derivation in Section 5.2):

$$\begin{aligned}W_e^* &= G^B \bar{U} \bar{U}^\dagger, & \mathbf{b}_e^* &= G^B (I - \bar{U} \bar{U}^\dagger) \bar{\mathbf{u}}, \\ W_d^* &= \bar{U} \bar{Y}^\dagger, & \mathbf{b}_d^* &= \bar{\mathbf{u}} - \bar{U} \bar{Y}^\dagger \bar{\mathbf{y}}.\end{aligned}$$

It can be seen that if a sufficient number of training data samples are provided such that \bar{U} is a full row rank matrix, i.e. $\bar{U} \bar{U}^\dagger = I$, then the encoder is able to represent exactly the PtO map G^B , i.e., $\Psi_e^*(\mathbf{u}^{\text{test}}) = G^B \mathbf{u}^{\text{test}} = \mathbf{y}^{\text{test}}$. In other words, the predicted PtO error estimation is zero, $\boldsymbol{\varepsilon}_{\mathbf{y}^{\text{test}}}^{\text{nPOP}} = 0$. At the same time, the decoder is able to represent the right inverse of G^B . Indeed, given a test PoI sample \mathbf{y}^{test} , we have

$$G^B \Psi_d^*(\mathbf{y}^{\text{test}}) = G^B (W_d^* \mathbf{y}^{\text{test}} + \mathbf{b}_d^*) = G^B \bar{U} \bar{Y}^\dagger \mathbf{y}^{\text{test}} + G^B \bar{\mathbf{u}} - G^B \bar{U} \bar{Y}^\dagger \bar{\mathbf{y}} = I \mathbf{y}^{\text{test}}.$$

It is important to note that the right inverse of G^B is not unique. In our nPOP approach, the decoder is concurrently satisfied with the following identity

$$(\Psi_d^*(Y) - U) Y^T = 0.$$

This identity indicates that the misfit of inverse solutions on training data is orthogonal to the column space of \bar{Y} . Additionally, it also implies the data-dependent nature (or data-driven property) of the decoder. On the other hand, the decoder is not guaranteed to be the left inverse of G^B , i.e., the inverted solution error can be written as

$$\boldsymbol{\varepsilon}_{\mathbf{u}^{\text{test}}}^{\text{nPOP}} = \|\Psi_d^*(\mathbf{y}^{\text{test}}) - \mathbf{u}^{\text{test}}\|_2^2 = \|(\bar{U} \bar{Y}^\dagger G^B - I) (\mathbf{u}^{\text{test}} - \bar{\mathbf{u}})\|_2^2.\tag{2}$$

In the ideal case, we expect nPOP to learn the unique left inverse of G^B , namely, $(G^B)^\dagger$, which is the best inverse map in the sense of solving least squares on the test sample. In that case, the error of inverse solutions reads

$$\left\| (G^B)^\dagger \mathbf{y}^{\text{test}} - \mathbf{u}^{\text{test}} \right\|_2^2 = \left\| \left((G^B)^\dagger G^B - I \right) \mathbf{u}^{\text{test}} \right\|_2^2.$$

It is worth noting that, although we can achieve full row rank matrices \bar{U}, \bar{Y} by data randomization technique [25], the inverse solution error Equation (2) can be very large.

2.2.2. Naïve autoencoder inverse-PtO learning approach nOP0

In contrast to the nPOP approach, we propose the nOP0 approach that learns inverse map with encoder and PtO map with decoder. The loss functions for nOP0 are defined as

$$\begin{aligned} \Psi_e^* &= \min \frac{1}{2} \|\Psi_e(Y) - U\|_F^2, \\ \Psi_d^* &= \min_{\Psi_d} \frac{1}{2} \|\Psi_d(\Psi_e^*(Y)) - Y\|_F^2. \end{aligned} \tag{nOP0}$$

For insights on nOP0, we analyze linear problems using a linear encoder for the inverse map $Z = \Psi_e(Y) = W_e Y + \mathbf{b}_e \mathbf{1}^T$ and a linear decoder for learning PtO map $\Psi_d(Z) = W_d Z + \mathbf{b}_d \mathbf{1}^T$. Substituting into eq. (nOP0), we have

$$\begin{aligned} W_e^*, \mathbf{b}_e^* &= \min_{W_e, \mathbf{b}_e} \frac{1}{2} \|W_e Y + \mathbf{b}_e \mathbf{1}^T - U\|_F^2, \\ W_d^*, \mathbf{b}_d^* &= \min_{W_d, \mathbf{b}_d} \frac{1}{2} \|W_d (W_e^* Y + \mathbf{b}_e^* \mathbf{1}^T) + \mathbf{b}_d \mathbf{1}^T - Y\|_F^2. \end{aligned} \tag{3}$$

By applying the first optimality condition, the optimal solutions for eq. (3) (see section 5.1 for full derivations) are

$$\begin{aligned} W_e^* &= \bar{U} \bar{Y}^\dagger, & \mathbf{b}_e^* &= \bar{\mathbf{u}} - \bar{U} \bar{Y}^\dagger \bar{\mathbf{y}}, \\ W_d^* &= \bar{Y} \bar{Z}^\dagger, & \mathbf{b}_d^* &= \bar{\mathbf{y}} - \bar{Y} \bar{Z}^\dagger \bar{\mathbf{u}}, \end{aligned}$$

where $\bar{Z} = \bar{U} \bar{Y}^\dagger \bar{Y}$. It can be seen that the encoder is exactly the same as the decoder of nPOP approach. Therefore, the inverse test error estimation is

$$\epsilon_{\mathbf{u}^{\text{test}}}^{\text{nOP0}} = \epsilon_{\mathbf{u}^{\text{test}}}^{\text{nPOP}} = \left\| (\bar{U} \bar{Y}^\dagger G^B - I) (\mathbf{u}^{\text{test}} - \bar{\mathbf{u}}) \right\|_2^2.$$

For the decoder, we first rewrite the predicted PtO solution as

$$\begin{aligned} \mathbf{y}^{\text{nOP0}} &= W_d^* \mathbf{u}^{\text{test}} + \mathbf{b}_d^* \mathbf{1}^T = \bar{Y} (\bar{Z}^\dagger - \bar{U}^\dagger + \bar{U}^\dagger) \mathbf{u}^{\text{test}} + \bar{\mathbf{y}} - \bar{Y} (\bar{Z}^\dagger - \bar{U}^\dagger + \bar{U}^\dagger) \bar{\mathbf{u}} \\ &= G \mathbf{u}^{\text{test}} + \bar{Y} (\bar{Z}^\dagger - \bar{U}^\dagger) (\mathbf{u}^{\text{test}} - \bar{\mathbf{u}}). \end{aligned}$$

It implies the the PtO map prediction error can be expressed as

$$\epsilon_{\mathbf{y}^{\text{test}}}^{\text{nOP0}} = \left\| \mathbf{y}^{\text{nOP0}} - \mathbf{y}^{\text{test}} \right\|_2^2 = \left\| \bar{Y} (\bar{Z}^\dagger - \bar{U}^\dagger) (\mathbf{u}^{\text{test}} - \bar{\mathbf{u}}) \right\|_2^2.$$

It can be seen that the decoder is not able to learn the PtO map G^B exactly even if a large amount of training data is available. Indeed, there is always a deviation due to error induced by the mismatch in inverted solutions obtained by the encoder solutions \bar{Z} and ground truth training data \bar{U} . Note that this error is inevitable since the encoder is not able to reconstruct the true U due to the ill-posed nature of the inverse map.

2.3. Model constrained autoencoder learning approaches

In this section, we present two model-constrained AutoEncoder approaches that incorporate the forward model \mathcal{G} into the loss function. As we shall show, *introducing the physics/discretization via the forward map provides better inverse surrogate models than naïve AutoEncoder approaches, presented in section 2.2. The model-constrained AutoEncoder approaches can also learn the PtO/forward maps with only one training data sample.*

2.3.1. Model-constrained autoEncoder PtO-inverse learning approach mcPOP

We propose a model-constrained AutoEncoder learning approach, mcPOP, in which the encoder learns the PtO map and the decoder learns the inverse map. As opposed to nPOP, mcPOP adds a model-constrained term that takes the predicted inverse solution from the decoder and reproduces the observation via the PtO map, G^B . The loss functions for mcPOP are expressed as

$$\begin{aligned}\Psi_e^* &= \min_{\Psi_e} \frac{1}{2} \|\Psi_e(U) - Y\|_F^2, \\ \Psi_d^* &= \min_{\Psi_d} \frac{1}{2} \|\Psi_d(\Psi_e^*(U)) - U\|_F^2 + \frac{\lambda}{2} \|B \circ \mathcal{G}(\Psi_d(\Psi_e^*(U))) - Y\|_F^2.\end{aligned}\tag{mcPOP}$$

Following the same procedure for linear problems using linear neural networks, the loss functions for mcPOP reads

$$\begin{aligned}W_e^*, \mathbf{b}_e^* &= \min_{W_e, \mathbf{b}_e} \frac{1}{2} \|W_e U + \mathbf{b}_e \mathbf{1}^T - Y\|_F^2, \\ W_d^*, \mathbf{b}_d^* &= \min_{W_d, \mathbf{b}_d} \frac{1}{2} \|W_d Z + \mathbf{b}_d \mathbf{1}^T - U\|_F^2 + \frac{\lambda}{2} \|G^B(W_d Z + \mathbf{b}_d \mathbf{1}^T) - Y\|_F^2,\end{aligned}\tag{4}$$

where $Z = W_e^* U + \mathbf{b}_e^* \mathbf{1}^T$. By apply the first optimality condition, the optimal solutions for eq. (4) for linear problems (derived in section 5.3) are

$$\begin{aligned}W_e^* &= G^B \bar{U} \bar{U}^\dagger, & \mathbf{b}_e^* &= G^B (I - \bar{U} \bar{U}^\dagger) \bar{\mathbf{u}}, \\ W_d^* &= (I + \lambda G^{BT} G^B)^{-1} (\bar{U} \bar{Y}^\dagger + \lambda G^{BT} \bar{Y} \bar{Y}^\dagger), \\ \mathbf{b}_d^* &= (I + \lambda G^{BT} G^B)^{-1} (\bar{\mathbf{u}} + \lambda G^{BT} \bar{\mathbf{y}} - (\bar{U} \bar{Y}^\dagger + \lambda G^{BT} \bar{Y} \bar{Y}^\dagger) \bar{\mathbf{y}}).\end{aligned}$$

It can be seen that the encoder is identical to the encoder obtained from nPOP. If a sufficient amount of data is available, i.e., \bar{U} is full row rank, the PtO map G^B can be learned well by the encoder, and thus $\varepsilon_{\mathbf{y}_{\text{test}}}^{\text{mcPOP}} = 0$. On the other hand, the inverse solutions obtained

by the decoder turn out the same as the solution of the Tikonov regularization approach. Specifically, given an observation sample \mathbf{y}^{test} , the inverse solution $\mathbf{u}^{\text{mcPOP}}$ can be derived as

$$\mathbf{u}^{\text{mcPOP}} = \left(I + \lambda G^{B^T} G^B \right)^{-1} \left(\bar{\mathbf{u}} + \lambda G^{B^T} \bar{\mathbf{y}} + \left(\bar{U} \bar{Y}^\dagger + \lambda G^{B^T} \bar{Y} \bar{Y}^\dagger \right) (\mathbf{y}^{\text{test}} - \bar{\mathbf{y}}) \right)$$

which is exactly the solution of the following Tikonov regularization problem

$$\min_{\mathbf{u}} \frac{1}{2} \|\mathbf{u} - \mathbf{u}^{\text{mc}}\|_2^2 + \frac{\lambda}{2} \|G^B \mathbf{u} - \mathbf{y}^{\text{test}}\|_2^2,$$

where

$$\mathbf{u}^{\text{mc}} = \bar{\mathbf{u}} + \bar{U} \bar{Y}^\dagger (\mathbf{y}^{\text{test}} - \bar{\mathbf{y}}) - \lambda G^{B^T} (I - \bar{Y} \bar{Y}^\dagger) (\mathbf{y}^{\text{test}} - \bar{\mathbf{y}}).$$

The corresponding error of predicted inverse solution $\mathbf{u}^{\text{mcPOP}}$ can be derived as

$$\begin{aligned} \epsilon_{\mathbf{u}^{\text{test}}}^{\text{mcPOP}} &= \|\mathbf{u}^{\text{mcPOP}} - \mathbf{u}^{\text{test}}\|_2^2 \\ &= \left\| \left(I + \lambda G^{B^T} G^B \right)^{-1} \left((\bar{U} \bar{Y}^\dagger G^B - I) (\mathbf{u}^{\text{test}} - \bar{\mathbf{u}}) + \lambda G^{B^T} (I - \bar{Y} \bar{Y}^\dagger) G^B (\mathbf{u}^{\text{test}} - \bar{\mathbf{u}}) \right) \right\|_2^2. \end{aligned}$$

It can be seen that if a sufficient amount of training data is given such that $\bar{Y} \bar{Y}^\dagger = I$, the error of predicted inverse solution $\mathbf{u}^{\text{mcPOP}}$ is lower by a factor of $\left(I + \lambda G^{B^T} G^B \right)^{-1}$ compared to nPOP and nOPO. This observation reveals the key benefit of the model-constrained AutoEncoder approach in learning the inverse map compared to the pure data-driven counterparts. However, we emphasize that the error of predicted inverse solution $\mathbf{u}^{\text{mcPOP}}$ is still data-dependent in that the inverse error is proportional to the distance $(\mathbf{u}^{\text{test}} - \bar{\mathbf{u}})$. In other words, it could have strongly bias to the mean of training data $\bar{\mathbf{u}}$. This bias could lead to poor generalization of the inverse surrogate model.

2.3.2. Model-constrained autoencoder inverse-PtO learning approach mcPOP

Conversely, we consider a model-constrained AutoEncoder inverse-PtO learning approach, mcOPO, in which the encoder learns the inverse map and the decoder learn the PtO map. Unlike nOPO, the encoder output is fed to the PtO model to reproduce observation data. As shown in mcPOP approach, this model-constrained strategy provides a better inverse solution surrogate model. Additionally, we learn the decoder by minimizing the misfit between decoder outputs and PtO maps, whose inputs are any outputs from encoder networks during training. The loss functions for mcOPO approach read

$$\begin{aligned} \Psi_e^* &= \min_{\Psi_e} \frac{1}{2} \|\Psi_e(Y) - U\|_F^2 + \frac{\lambda}{2} \|B \circ \mathcal{G}(\Psi_e(Y)) - Y\|_F^2, \\ \Psi_d^* &= \min_{\Psi_d} \frac{1}{2} \|\Psi_d(\Psi_e^*(Y)) - B \circ \mathcal{G}(\Psi_e^*(Y))\|_F^2. \end{aligned} \tag{mcOPO}$$

Similarly to previous analysis for other approaches, we apply to the linear problems with linear encoder and decoder neural networks, the loss functions for mcOPO are given as

$$\begin{aligned}
W_e^*, \mathbf{b}_e^* &= \min_{W_e, \mathbf{b}_e} \frac{1}{2} \|W_e Y + \mathbf{b}_e \mathbf{1}^T - U\|_F^2 + \frac{\lambda}{2} \|G^B (W_e Y + \mathbf{b}_e \mathbf{1}^T) - Y\|_F^2, \\
W_d^*, \mathbf{b}_d^* &= \min_{W_d, \mathbf{b}_d} \frac{1}{2} \|W_d (W_e^* Y + \mathbf{b}_e^* \mathbf{1}^T) + \mathbf{b}_d \mathbf{1}^T - G^B (W_e^* Y + \mathbf{b}_e^* \mathbf{1}^T)\|_F^2.
\end{aligned} \tag{5}$$

By applying the first optimality condition, the optimal solutions for eq. (5) as derived in section 5.4 are

$$\begin{aligned}
W_e^* &= (I + \lambda G^{B^T} G^B)^{-1} (\bar{U} \bar{Y}^\dagger + \lambda G^{B^T} \bar{Y} \bar{Y}^\dagger), \\
\mathbf{b}_e^* &= (I + \lambda G^{B^T} G^B)^{-1} (\bar{\mathbf{u}} + \lambda G^{B^T} \bar{\mathbf{y}} - (\bar{U} \bar{Y}^\dagger + \lambda G^{B^T} \bar{Y} \bar{Y}^\dagger) \bar{\mathbf{y}}), \\
W_d^* &= G^B \bar{Z} \bar{Z}^\dagger, \quad \mathbf{b}_d^* = G^B (I - \bar{Z} \bar{Z}^\dagger) \bar{\mathbf{z}},
\end{aligned}$$

where

$$\begin{aligned}
\bar{\mathbf{z}} &= (I + \lambda G^{B^T} G^B)^{-1} (\bar{\mathbf{u}} + \lambda G^{B^T} \bar{\mathbf{y}}), \\
\bar{Z} &= (I + \lambda G^{B^T} G^B)^{-1} [\bar{U} \bar{Y}^\dagger \bar{Y} + \lambda G^{B^T} \bar{Y}].
\end{aligned}$$

It can be seen that the encoder learns exactly the same inverse map as the decoder in **mcPOP** approach. Therefore, we have $\boldsymbol{\varepsilon}_{\mathbf{u}^{\text{test}}}^{\text{mcOP0}} = \boldsymbol{\varepsilon}_{\mathbf{u}^{\text{test}}}^{\text{mcPOP}}$. On the other hand, for the learned decoder, we can see that as long as \bar{Z} , or equivalent \bar{Y} , is full row rank, the PtO map G^B can be learned well by the decoder. Unlike, the naïve data-driven approaches **nPOP** where we need \bar{U} is full row rank or **nOP0** where it is impossible to construct the exact inverse map, **mcPOP** can learn exactly the PtO map with only one observation sample, i.e.,

$$\Psi_d^* (\mathbf{u}^{\text{test}}) = G^B \mathbf{u}^{\text{test}} = \mathbf{y}^{\text{test}}. \tag{6}$$

Indeed, the condition of full row rank Y can be satisfied in two ways: a sufficient amount of training data is given, or columns of \bar{Y} are simply randomized observation samples from a single observation sample [25]. Consequently, we have a zero PtO error estimation, $\boldsymbol{\varepsilon}_{\mathbf{y}^{\text{test}}}^{\text{mcOP0}} = 0$ (at least with high probability).

2.3.3. Model-constrained autoencoder inverse-forward learning approach **mcOP0-Full**

Observed the advantages of **mcOP0** approach on learning the PtO map by only one single training sample from eq. (6), we propose a model-constrained AutoEncoder inverse-forward learning approach, **mcOP0-Full**, in which the encoder learns the inverse map and the decoder learn the forward map (parameter to full solution of the PDE). The loss functions for **mcOP0-Full** are

$$\begin{aligned}
\Psi_e^* &= \min_{\Psi_e} \frac{1}{2} \|U - \Psi_e(Y)\|_F^2 + \frac{\lambda}{2} \|Y - B \circ \mathcal{G}(\Psi_e(Y))\|_F^2, \\
\Psi_d^* &= \min_{\Psi_d} \frac{1}{2} \|\mathcal{G}(\Psi_e^*(Y)) - \Psi_d(\Psi_e^*(Y))\|_F^2.
\end{aligned} \tag{mcOP0-Full}$$

Following the similar procedure in section 2.3.2 for linear problems using linear neural networks, the optimal solutions for **mcOPO-Full** are

$$\begin{aligned} W_e^* &= (I + \lambda G^{B^T} G^B)^{-1} (\bar{U}\bar{Y}^\dagger + \lambda G^{B^T} \bar{Y}\bar{Y}^\dagger), \\ \mathbf{b}_e^* &= (I + \lambda G^{B^T} G^B)^{-1} (\bar{\mathbf{u}} + \lambda G^{B^T} \bar{\mathbf{y}} - (\bar{U}\bar{Y}^\dagger + \lambda G^{B^T} \bar{Y}\bar{Y}^\dagger) \bar{\mathbf{y}}), \\ W_d^* &= G\bar{Z}\bar{Z}^\dagger, \quad \mathbf{b}_d^* = G(I - \bar{Z}\bar{Z}^\dagger) \bar{\mathbf{z}}, \end{aligned}$$

where

$$\begin{aligned} \bar{\mathbf{z}} &= (I + \lambda G^{B^T} G^B)^{-1} (\bar{\mathbf{u}} + \lambda G^{B^T} \bar{\mathbf{y}}), \\ \bar{Z} &= (I + \lambda G^{B^T} G^B)^{-1} [\bar{U}\bar{Y}^\dagger \bar{Y} + \lambda G^{B^T} \bar{Y}]. \end{aligned}$$

It can be seen that the encoder is identical to the one obtained by **mcPOP**, **mcOPO**, thus the inverse error estimate is $\boldsymbol{\varepsilon}_{\mathbf{u}_{\text{test}}}^{\text{mcOPO-Full}} = \boldsymbol{\varepsilon}_{\mathbf{u}_{\text{test}}}^{\text{mcOPO}} = \boldsymbol{\varepsilon}_{\mathbf{u}_{\text{test}}}^{\text{mcPOP}}$. Meanwhile, the decoder is able to learn the PDEs linear solver G by only one single observation sample in a similar way that **mcOPO** approach does, i.e., $\boldsymbol{\varepsilon}_{\boldsymbol{\omega}_{\text{test}}}^{\text{mcOPO-Full}} = 0$.

2.4. Model-constrained Tikhonov autoencoder approaches

As discussed in the naïve and model-constrained approaches, **nPOP**, **nOPO**, **mcPOP**, **mcOPO**, and **mcOPO-Full**, the performance of learned inverse surrogate models depends on the training data samples. In our previous work [59], we proposed **TNet**, model-constrained Tikhonov neural network, which can learn the inverse map with much fewer training samples than naïve and model-constrained approaches. Furthermore, shown above for **mcOPO** and **mcOPO-Full** with linear models, we can learn the exact PtO and forward map with only one training observation sample. We now propose **TAEN** and **TAEN-Full** approaches which, as will be shown, are able to learn the inverse and PtO/forward maps with only one training sample. Further, we emphasize that **TAEN** and **TAEN-Full** require only the “label” part, namely \mathbf{y} , of the training samples and the prior mean of the PoI, \mathbf{u}_0 , while no ground truth PoI is needed.²

2.4.1. Model-constrained Tikhonov autoencoder inverse-PtO learning approach **TAEN**

The schematic of **TAEN** is presented in fig. 1. A sequential learning strategy is applied to learn the encoder and decoder in two phases. In **Phase 1**, at every epoch during training, we randomize the observational data with noise $\boldsymbol{\varepsilon} \sim \mathcal{N}(0, \varepsilon^2 [\mathbf{diag}(\mathbf{y})]^2)$ which is added to the observation data \mathbf{y} to generate randomized observation samples. The randomized data is then fed into the encoder network Ψ_e to predict the inverse solution \mathbf{u}^* . The predicted inverse \mathbf{u}^* is passed to the PtO map $B \circ \mathcal{G}$ to predict the observation data $B\boldsymbol{\omega}^*$. We minimize the encoder loss \mathcal{L}_e for the encoder network. In **Phase 2**, we randomize observations and pass through the already-trained encoder network to produce inverse solutions \mathbf{u}^* . Then, \mathbf{u}^*

²Tikhonov-type of learning method is thus suitable for most practical situations where we do not have training pairs (\mathbf{u}, \mathbf{y}) , but only the label \mathbf{y} parts.

is treated as inputs to both the decoder network Ψ_d to produce \mathbf{y}^* and PtO map to produce $B\boldsymbol{\omega}^*$. The decoder loss \mathcal{L}_d is then minimized to find optimal decoder parameters. In other words, in **Phase 2**, we can consider the encoder as the generative engine that generates physics samples \mathbf{u}^* to train the PtO surrogate model. The loss functions for TAEN from fig. 1 are given as

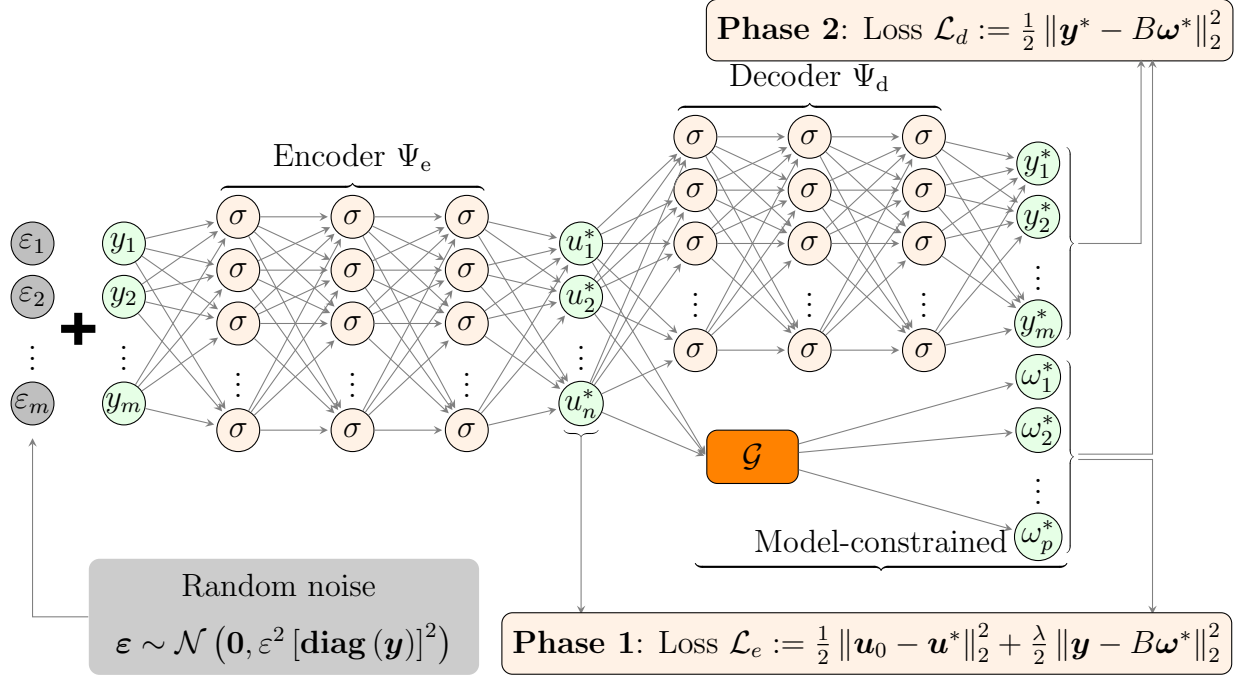


Figure 1: The schematic of TAEN approach. A sequential learning strategy is applied to learn the encoder and decoder in two phases. In **Phase 1**, at every epoch during training, we randomize the observation data with noise $\boldsymbol{\varepsilon} \sim \mathcal{N}(0, \varepsilon^2 [\mathbf{diag}(\mathbf{y})]^2)$ which is added to the observation data \mathbf{y} to generate randomized observation samples. The randomized data is then fed into the encoder network Ψ_e to predict the inverse solution \mathbf{u}^* . The predicted inverse \mathbf{u}^* is passed to the PtO map $B \circ \mathcal{G}$ to predict the observation data $B\boldsymbol{\omega}^*$. We minimize the encoder loss \mathcal{L}_e for the optimal encoder network. In **Phase 2**, we randomize observations and pass through the pre-trained encoder network to produce inverse solutions \mathbf{u}^* . Then, \mathbf{u}^* is treated as inputs to both the decoder network Ψ_d to produce \mathbf{y}^* and PtO map to produce $B\boldsymbol{\omega}^*$. The decoder loss \mathcal{L}_d is then minimized to find optimal decoder parameters.

$$\begin{aligned} \Psi_e^* &= \min_{\Psi_e} \frac{1}{2} \|\Psi_e(Y) - \mathbf{u}_0 \mathbf{1}^T\|_F^2 + \frac{\lambda}{2} \|B \circ \mathcal{G}(\Psi_e(Y)) - Y\|_F^2, \\ \Psi_d^* &= \min_{\Psi_d} \frac{1}{2} \|\Psi_d(\Psi_e^*(Y)) - B \circ \mathcal{G}(\Psi_e^*(Y))\|_F^2. \end{aligned} \quad (\text{TAEN})$$

For linear problems and linear networks (see previous sections), the loss functions for TAEN becomes

$$\begin{aligned} W_e^*, \mathbf{b}_e^* &= \min_{W_e, \mathbf{b}_e} \frac{1}{2} \|W_e Y + \mathbf{b}_e \mathbf{1}^T - \mathbf{u}_0 \mathbf{1}^T\|_F^2 + \frac{\lambda}{2} \|G^B (W_e Y + \mathbf{b}_e \mathbf{1}^T) - Y\|_F^2, \\ W_d^*, \mathbf{b}_d^* &= \min_{W_d, \mathbf{b}_d} \frac{1}{2} \|\Psi_d (W_e^* Y + \mathbf{b}_e^* \mathbf{1}^T) - G^B (W_e^* Y + \mathbf{b}_e^* \mathbf{1}^T)\|_F^2. \end{aligned} \quad (7)$$

The main difference in TAEN compared to mcOPO is now $U = \mathbf{u}_0 \mathbf{1}^T$. It is straightforward to achieve the optimal solutions for eq. (7) (as derived in section 5.5):

$$\begin{aligned} W_e^* &= (I + \lambda G^{B^T} G^B)^{-1} (\lambda G^{B^T} \bar{Y} \bar{Y}^\dagger), \\ \mathbf{b}_e^* &= (I + \lambda G^{B^T} G^B)^{-1} (\mathbf{u}_0 + \lambda G^{B^T} \bar{\mathbf{y}} - \lambda G^{B^T} \bar{Y} \bar{Y}^\dagger \bar{\mathbf{y}}), \\ W_d^* &= G^B \bar{Z} \bar{Z}^\dagger, \quad \mathbf{b}_d^* = G^B (I - \bar{Z} \bar{Z}^\dagger) \bar{\mathbf{z}}, \end{aligned}$$

where

$$\begin{aligned} \bar{\mathbf{z}} &= (I + \lambda G^{B^T} G^B)^{-1} (\mathbf{u}_0 + \lambda G^{B^T} \bar{\mathbf{y}}), \\ \bar{Z} &= (I + \lambda G^{B^T} G^B)^{-1} (\lambda G^{B^T} \bar{Y}). \end{aligned}$$

The TAEN inverse solution obtained by the encoder network for an observation test sample, \mathbf{y}^{test} , is given by

$$\mathbf{u}^{\text{TAEN}} = (I + \lambda G^{B^T} G^B)^{-1} (\mathbf{u}_0 + \lambda G^{B^T} \bar{\mathbf{y}} + \lambda G^{B^T} \bar{Y} \bar{Y}^\dagger (\mathbf{y}^{\text{test}} - \bar{\mathbf{y}}))$$

which is exactly the inverse solution of the following linear Tikhonov regularization problem

$$\min_{\mathbf{u}} \frac{1}{2} \|\mathbf{u} - \mathbf{u}_0\|_2^2 + \frac{\lambda}{2} \|G^B \mathbf{u} - \mathbf{y}^{\text{test}}\|_2^2.$$

Therefore, the error of inverse solutions obtained from the TAEN encoder network is

$$\begin{aligned} \epsilon_{\mathbf{u}^{\text{test}}}^{\text{TAEN}} &= \|\mathbf{u}^{\text{TAEN}} - \mathbf{u}^{\text{test}}\|_2^2 \\ &= \left\| \left(I + \lambda G^{B^T} G^B \right)^{-1} \left((\mathbf{u}_0 - \mathbf{u}^{\text{test}}) + \lambda G^{B^T} (I - \bar{Y} \bar{Y}^\dagger) (\mathbf{y}^{\text{test}} - \bar{\mathbf{y}}) \right) \right\|_2^2. \end{aligned}$$

It can be seen that as long as \bar{Y} is full row rank, which can be obtained with high probability by having large number of randomization observation samples [25], the error can be written as (again with high probability)

$$\epsilon_{\mathbf{u}^{\text{test}}}^{\text{TAEN}} = \left\| \left(I + \lambda G^{B^T} G^B \right)^{-1} (\mathbf{u}_0 - \mathbf{u}^{\text{test}}) \right\|_2^2 \leq \|\mathbf{u}_0 - \mathbf{u}^{\text{test}}\|_2^2,$$

independent of the single training sample. On the other hand, similar to the decoder of mcOPO, it can be shown that the TAEN decoder network is able to learn the PtO map exactly, $\epsilon_{\mathbf{y}^{\text{test}}}^{\text{TAEN}} = 0$, with only one observation training sample.

2.4.2. Model-constrained Tikhonov autoencoder inverse-forward learning approach **TAEN-Full**

Inspired by advantages of **TAEN** and **mcOPO-Full**, we propose a new approach, **TAEN-Full**, where the encoder learns the inverse Tikhonov regularization solver and the decoder learns the forward map (parameter to solution of PDEs). We construct the loss for **TAEN-Full** as

$$\begin{aligned}\Psi_e^* &= \min_{\Psi_e} \frac{1}{2} \|\Psi_e(Y) - \mathbf{u}_0 \mathbf{1}^T\|_F^2 + \frac{\lambda}{2} \|B \circ \mathcal{G}(\Psi_e(Y)) - Y\|_F^2, \\ \Psi_d^* &= \min_{\Psi_d} \frac{1}{2} \|\Psi_d(\Psi_e(Y)) - \mathcal{G}(\Psi_e(Y))\|_F^2.\end{aligned}\tag{TAEN-Full}$$

Analogous to other approaches, in the context of linear problems using linear autoencoder networks, the optimal solutions for encoder and decoder networks are

$$\begin{aligned}W_e^* &= (I + \lambda G^{BT} G^B)^{-1} (\lambda G^{BT} \bar{Y} \bar{Y}^\dagger), \\ \mathbf{b}_e^* &= (I + \lambda G^{BT} G^B)^{-1} (\mathbf{u}_0 + \lambda G^{BT} \bar{\mathbf{y}} - \lambda G^{BT} \bar{Y} \bar{Y}^\dagger \bar{\mathbf{y}}), \\ W_d^* &= G \bar{Z} \bar{Z}^\dagger, \quad \mathbf{b}_d^* = G (I - \bar{Z} \bar{Z}^\dagger) \bar{\mathbf{z}},\end{aligned}$$

where

$$\begin{aligned}\bar{\mathbf{z}} &= (I + \lambda G^{BT} G^B)^{-1} (\mathbf{u}_0 + \lambda G^{BT} \bar{\mathbf{y}}), \\ \bar{Z} &= (I + \lambda G^{BT} G^B)^{-1} (\lambda G^{BT} \bar{Y}).\end{aligned}$$

It can be seen that the encoder network of **TAEN-Full** is exactly the same as encoder network of **TAEN**, and thus $\epsilon_{\mathbf{u}^{\text{test}}}^{\text{TAEN-Full}} = \epsilon_{\mathbf{u}^{\text{test}}}^{\text{TAEN}}$. Similar to the decoder of **mcOPO-Full**, the decoder network of **TAEN-Full** is able to learn the forward map exactly with only one observation training sample, i.e., $\epsilon_{\omega^{\text{test}}}^{\text{TAEN-Full}} = 0$.

For clarity, we summarize the error estimations of the proposed approaches in table 1 and whether or not an approach can learn the PtO/forward and inverse map with only one training sample.

Table 1: Summary of test error estimations obtained from various approaches for solving linear problems using linear encoder and decoder networks.

Approaches	PtO/forward error $\epsilon_{\mathbf{y}^{\text{test}}} / \epsilon_{\omega^{\text{test}}}$	Inverse error $\epsilon_{\mathbf{u}^{\text{test}}}$	Ability to learn with 1 sample
nPOP	0	$\ (\bar{U} \bar{Y}^\dagger G^B - I) (\mathbf{u}^{\text{test}} - \bar{\mathbf{u}})\ _2^2$	None
nOPO	inevitably > 0		None
mcPOP	0	$\leq \ (\bar{U} \bar{Y}^\dagger G^B - I) (\mathbf{u}^{\text{test}} - \bar{\mathbf{u}})\ _2^2$	Only PtO
mcOPO(-Full)	0		Only PtO/forward
TAEN(-Full)	0	$\leq \ \mathbf{u}^{\text{test}} - \mathbf{u}_0\ _2^2$	All

2.5. Simultaneous training strategy for encoder and decoder networks

In this section, we examine the drawbacks of simultaneous training compared to sequential training strategies. Although these drawbacks are common across all methodologies, we provide an analysis only for the nPOP framework, as it provides a clear picture of the drawbacks. Specifically, we analyze a case where both the encoder and decoder neural networks of nPOP undergo simultaneous training using the same training dataset (U, Y) . In this scenario, we introduce an additional hyperparameter β to achieve an appropriate balance between the encoder and decoder loss functions. The loss function can be expressed as

$$\Psi_e^*, \Psi_d^* = \min_{\Psi_e, \Psi_d} \frac{1}{2} \|\Psi_e(U) - Y\|_F^2 + \frac{\beta}{2} \|\Psi_d(\Psi_e(U)) - U\|_F^2, \quad (8)$$

To gain insights into how different the simultaneous training strategy is compared to the sequential training counterpart, we analyze the same linear problems using linear encoder and decoder networks. By deriving the first optimality condition for eq. (8), we can obtain the optimal weight and bias for the encoder and decoder networks as follows (see section 5.6 for full derivation):

$$\begin{aligned} W_e^* &= (I + \beta W_d^{*T} W_d^*)^{-1} (G^B \bar{U} \bar{U}^\dagger + \beta W_d^{*T} \bar{U} \bar{U}^\dagger), & \mathbf{b}_e^* &= \bar{\mathbf{y}} - W_e^* \bar{\mathbf{u}}, \\ W_d^* &= \bar{U} (W_e^* \bar{U})^\dagger, & \mathbf{b}_d^* &= \bar{\mathbf{u}} - W_d^* \bar{\mathbf{y}}, \\ W_e^* \bar{U} \bar{U}^T &= W_e^* W_d^* W_e^* \bar{U} \bar{U}^T \end{aligned}$$

The first drawback emerges from the difficulty in deriving closed-form solutions for the optimal parameters W_e^* , \mathbf{b}_e^* , W_d^* , and \mathbf{b}_d^* since W_e^* is a nonlinear function of W_d^* . In other words, even with linear problems, we might need to use some iterative algorithm to obtain a solution. Furthermore, even with sufficient training data, such that $\bar{U} \bar{U}^\dagger = I$, the encoder network becomes

$$W_e^* = (I + \beta W_d^{*T} W_d^*)^{-1} (G^B + \beta W_d^{*T}), \quad \mathbf{b}_e^* = \bar{\mathbf{y}} - W_e^* \bar{\mathbf{u}},$$

and in this case, it is still not clear how to train the optimal encoder to recover the exact linear PtO map G^B . As a result, the decoder accuracy will be affected by the outputs from the inaccuracy of the encoder network. The second drawback of the simultaneous training strategy is that tuning the hyperparameter β for the encoder loss and decoder loss is required and problem-dependent, in addition to having a larger training problem to solve. In a special case of $\beta = 1$, one of the optimal solutions W_e^* , \mathbf{b}_e^* , W_d^* , \mathbf{b}_d^* for eq. (8) is indeed identical to the one obtained by the sequential training strategy in section 2.2.1,

$$W_e^* = G^B \bar{U} \bar{U}^\dagger, \quad \mathbf{b}_e^* = G^B (I - \bar{U} \bar{U}^\dagger) \bar{\mathbf{u}}, \quad W_d^* = \bar{U} \bar{Y}^\dagger, \quad \mathbf{b}_d^* = \bar{\mathbf{u}} - \bar{U} \bar{Y}^\dagger \bar{\mathbf{y}}.$$

Thus, the simultaneous training strategy (even with the identical linear setting), the encoder is not guaranteed to recover the exact PtO map. We also present a similar derivation for nOPO in section 5.7 which shows two similar drawbacks of simultaneous training strategy.

2.6. Some theoretical justification for the generalization capability with randomization for nonlinear problems

In this section, we provide theoretical justification for why randomization could facilitate accurate generalization even with one initial training sample. We shall focus on the sequential eq. (TAEN) approach in section 2.4, but our discussion is applicable to the other methods as well. Recall from our previous work [59, Theorem 4.3] that randomization induces a regularization, with the noise variance as the regularization parameter, on the regularity of the encoder neural network Ψ_e^* (the first subequation of eq. (TAEN)) and its difference with the true inverse operator up to second order derivatives. We now present some further theoretical justification from a probabilistic angle.

With randomization, the randomized data is distributed as

$$\mathbf{y}^{rand} \sim \mathcal{N}(\mathbf{y}, \varepsilon^2 [\mathbf{diag}(\mathbf{y})]^2),$$

where \mathbf{y} is the data before randomization. We assume that the prior distribution of the PoI³ is a Gaussian:

$$\mathbf{u} \sim \mathcal{N}(\mathbf{u}_0, I),$$

which is push-forwarded to the underlying distribution of the observational data \mathbf{y}^{obs} via the forward map $\mathcal{G}(\mathbf{u})$ as⁴

$$\mathbf{y}^{obs} \sim B \circ \mathcal{G}_{\#} \mathcal{N}(\mathbf{u}_0, I).$$

We conclude that if the randomization is such that the true data distribution $B \circ \mathcal{G}_{\#} \mathcal{N}(\mathbf{u}_0, I)$ is absolutely continuous with respect to the randomized data distribution $\mathcal{N}(\mathbf{y}, \varepsilon^2 [\mathbf{diag}(\mathbf{y})]^2)$ —that is, the support of the former is contained in the support of the latter—randomization could explore unseen data/information that is not contained in the original data set (be it one training sample or more). Together with the aforementioned regularization effect to ensure the encoder to closely matches the inverse map (the first term of the first subequation in eq. (TAEN)), and the push forward measure $\Psi_{e\#}^* \mathcal{N}(\mathbf{y}, \varepsilon^2 [\mathbf{diag}(\mathbf{y})]^2)$ to be similar to the prior distribution of PoI $\mathcal{N}(\mathbf{u}_0, I)$ so that the composition of the push forward measures $B \circ \mathcal{G}_{\#} \Psi_{e\#}^* \mathcal{N}(\mathbf{y}, \varepsilon^2 [\mathbf{diag}(\mathbf{y})]^2)$ is close to the randomized data distribution $\mathcal{N}(\mathbf{y}, \varepsilon^2 [\mathbf{diag}(\mathbf{y})]^2)$ (the second term of the first subequation in eq. (TAEN)). Here, the closeness is in the minimal Kullback-Leibler (KL) divergence sense. When that happens, the true data distribution $B \circ \mathcal{G}_{\#} \mathcal{N}(\mathbf{u}_0, I)$ is absolutely continuous with respect to $B \circ \mathcal{G}_{\#} \Psi_{e\#}^* \mathcal{N}(\mathbf{y}, \varepsilon^2 [\mathbf{diag}(\mathbf{y})]^2)$. In other words, the randomized data distribution, when push-forwarded through the encoder Ψ_e^* and then the forward map, has minimal KL divergence change so as to cover the true data distribution.

Next, the second optimization problem (the second subequation in eq. (TAEN)) in the TAEN approach is to ensure that the randomized data distribution, when push-forwarded through the encoder Ψ_e^* and then the decoder Ψ_d^* , is indifferent (again in the minimal KL

³For the simplicity of the presentation we use identity covariance here, but the result is also valid for arbitrary prior covariance matrix.

⁴It typically comes with some additive noise as in section 2.1, but for the clarity, we ignore it here.

divergence) to $B \circ \mathcal{G}_{\#} \Psi_{e\#}^* \mathcal{N}(\mathbf{y}, \varepsilon^2 [\mathbf{diag}(\mathbf{y})]^2)$. In other words, with appropriate conditions on the autoencoder and the forward map, it can be shown that the optimization problem in the second subequation in eq. (TAEN) is equivalent to minimizing the KL divergence between $\Psi_{d\#}^* \Psi_{e\#}^* \mathcal{N}(\mathbf{y}, \varepsilon^2 [\mathbf{diag}(\mathbf{y})]^2)$ and $B \circ \mathcal{G}_{\#} \Psi_{e\#}^* \mathcal{N}(\mathbf{y}, \varepsilon^2 [\mathbf{diag}(\mathbf{y})]^2)$. As argued above, since the true data distribution $B \circ \mathcal{G}_{\#} \mathcal{N}(\mathbf{u}_0, I)$ is absolutely continuous with the latter, so is it with the former. It follows that TAEN can generalize well when equipped with the right amount of random noise level.

What remains is to estimate such a right random level for a particular problem under consideration. This is clearly problem-dependent as it depends on the forward map and the architecture of the autoencoder. Numerically (see fig. 7 and fig. 14), we observe the generalization capability is robust to a wide range of noise level. This could be due to the compactness [12, 11, 10] nature of the forward map. Below we provide a theoretical insight on why too small or too large noise levels may not help improve generalization capability of TAEN. Two observations/comments are in order.

1. If the true data distribution $B \circ \mathcal{G}_{\#} \mathcal{N}(\mathbf{u}_0, I)$ is not absolutely continuous with respect to the randomized data distribution $\mathcal{N}(\mathbf{y}, \varepsilon^2 [\mathbf{diag}(\mathbf{y})]^2)$, which corresponds to the small noise levels, then the generalization capability of our approach is limited.
2. If the true data distribution $B \circ \mathcal{G}_{\#} \mathcal{N}(\mathbf{u}_0, I)$ is absolutely continuous with respect to the randomized data distribution $\mathcal{N}(\mathbf{y}, \varepsilon^2 [\mathbf{diag}(\mathbf{y})]^2)$, but the noise level is too high, then the generalization capability of our approach is also limited.

The poor generalization with the aforementioned two extreme scenarios will be numerically observed for both heat and Navier-Stokes equation in fig. 7 and fig. 14, respectively. The reason for both cases is that the trained network does not see sufficient information covered in the true data distribution $B \circ \mathcal{G}_{\#} \mathcal{N}(\mathbf{u}_0, I)$. *This is a direct consequence of the concentration of measure phenomena.* In particular, with high probability, the distance between the randomized data \mathbf{y}^{rand} and the observational data \mathbf{y}^{obs} scales like [86]

$$\|\mathbf{y}^{rand} - \mathbf{y}^{obs}\| \approx \varepsilon \sqrt{m} \|\mathbf{y}\|.$$

Thus, if ε is too small, the randomized data is concentrated around the initial data \mathbf{y} . On the other hand, when ε is large, the randomized data is concentrated in the neighborhood of a hypersphere shell of radius approximately $\varepsilon \sqrt{m} \|\mathbf{y}\|$ away from the initial data. In either case, the randomized data is not sufficiently rich for generalization purposes.

We conclude this section with a remark that the above theoretical arguments can be made rigorous with additional assumptions on the forward map, the training procedure, and the autoencoder architecture. Since such a rigorous analysis does not provide additional insights, but simply an exercise, we choose not to pursue it here.

3. Numerical results

We begin by outlining the training and testing configurations for our proposed approaches for solving forward and inverse problems, focusing on two PDEs: the heat equation in sec-

tion 3.1 and the Navier-Stokes equation in section 3.2. table 2 summarizes the specifications for neural network architectures, training settings, data sets, etc.

Table 2: Summary of training parameters for learning forward and inverse problems in section 3.1 and section 3.2.

Network	Architecture	1 layer with 5000 neurons
	Activation function	ReLU
	Weight initializer	$\mathcal{N}(0, 0.02)$
	Bias initializer	$\mathbf{0}$
	Random seed	100
Training	Optimizer	ADAM
	Learning rate	10^{-3}
	Batch size	$n_t = 100$
Data	Train data	100 samples (drawn independently)
	Test data	500 samples (drawn independently)
	Train random seed	18
	Test random seed	28
Precision	Double precision	

Data generation. Our training dataset comprises 100 paired samples of PoIs and their corresponding clean observations $\mathbf{y}^{\text{clean}}$, which are subsequently corrupted to \mathbf{y}^{test} according to eq. (9). We consider two training cases: Case I - single-sample training; and Case II - 100-sample training. In case I, we replicate the randomly chosen sample to create a set of 100 identical samples. In case II, we use all different 100 training samples. For evaluation purposes, we utilize a test dataset of 500 sample pairs, corrupted with noise level δ as eq. (9), to benchmark different approaches. The Tikhonov inverse solutions are computed using the standard BFGS optimization algorithm [60] available in Jax-Optax [9].

Two stages of adding noise. For each sample regardless of case I or case II, we corrupt noise at two stages in our experimental framework. Initially, we introduce a noise level δ to the clean synthetic data to simulate real-world observations:

$$\mathbf{y}^{\text{test}} = \mathbf{y}^{\text{clean}} + \boldsymbol{\delta} \odot \mathbf{y}^{\text{clean}}, \quad \boldsymbol{\delta} \sim \mathcal{N}(0, \delta^2 \mathbf{I}), \quad (9)$$

where \odot represents element-wise multiplication, $\mathbf{y}^{\text{clean}}$ denotes the noise-free data generated by the forward solver, and $\mathbf{I} \in \mathbb{R}^{m \times m}$ is the $m \times m$ identity matrix. Subsequently, we perform the data randomization technique. Specifically, for each epoch during training, for mcOPO, mcOPO-Full, TAEN and TAEN-Full methods, we apply an additional noise level ε on-the-fly to the simulated real-world data \mathbf{y}^{test} :

$$\tilde{\mathbf{y}}^{\text{rand}} = \mathbf{y}^{\text{test}} + \boldsymbol{\varepsilon}, \quad \boldsymbol{\varepsilon} \sim \mathcal{N}(0, \varepsilon^2 [\mathbf{diag}(\mathbf{y}^{\text{test}})]^2), \quad (10)$$

where $[\cdot]^2$ denotes the elementwise square operation. In practice, we generate a randomized sample as follows, drawing standard Gaussian random samples ζ and then point-wise

multiplication with \mathbf{y}^{test} to generate noise realizations, i.e.,

$$\tilde{\mathbf{y}}^{\text{rand}} = \mathbf{y}^{\text{test}} + \boldsymbol{\zeta} \odot \mathbf{y}^{\text{test}}, \quad \boldsymbol{\zeta} \sim \mathcal{N}(0, \varepsilon^2 \mathbf{I}).$$

Specifically, we draw 100 new noise realizations $\boldsymbol{\varepsilon}$ per epoch and add them to 100 observation samples in both case I and case II. For the **nPOP** and **mcPOP** methods, we retain only the base noise level δ , excluding the additional randomization noise level ε , as these approaches utilize PoIs as input data. We made this choice considering that introducing excessive noise to PoIs might lead to non-physical or implausible PoI samples. Additionally, for the **nOPO** approach, our experimental results show that it exhibits superior performance without the data randomization technique. Thus, we also do not apply ε noise level for the **nOPO** approach.

Accuracy metric. To evaluate the performance of the learned inverse and PtO/forward mappings for all approaches, we compare the overall accuracy over 500 independent test samples. For the inverse mapping, we employ two error metrics: one based on the average pointwise absolute error values

$$E_{abs,j} = \frac{1}{500} \sum_{i=1}^{500} \left| u_j^{i,\text{pred}} - u_j^{i,\text{true}} \right| \quad j = 1, \dots, n, \quad (11)$$

and another using the average relative Euclidean norm error

$$E_{rel} = \frac{1}{500} \sum_{i=1}^{500} \frac{\|\mathbf{u}^{i,\text{pred}} - \mathbf{u}^{i,\text{true}}\|_2^2}{\|\mathbf{u}^{i,\text{true}}\|_2^2}, \quad (12)$$

where i indexes the sample number, j represents the component index of the discretized sample vector, and n is the number of spatial grid points. The superscripts “pred” and “true” stand for the solution predicted by the neural network and the ground truth parameters of interest, respectively. For the learned PtO mapping, we assess accuracy using the average relative error between predicted observations \mathbf{y}^{pred} and true observations \mathbf{y}^{true} following eq. (12). Since **mcOPO-Full** and **TAEN-Full** approaches are developed to learn the forward map predicting the complete solution $\boldsymbol{\omega}$, we maintain consistency in comparison by applying the same accuracy metric on $\mathbf{y} = B\boldsymbol{\omega}$ across all approaches.

Training settings. For both heat equation and Navier-Stokes equation, we use a shallow neural network having one hidden layer with 5000 ReLU neurons for both encoder and decoder neural networks. In our previous work [59], we verified that a dense feed-forward neural network architecture with multiple layers, in small data regimes, performs poorly due to the vanishing gradient and/or the bias-variance trade-off issues. We thus focus on neural networks with a single hidden layer and this is sufficient to demonstrate the proposed AutoEncoder frameworks. Regarding the optimization algorithm, the default **ADAM** [42] optimizer in **JAX** [9] is used. To ensure fairness across all numerical experiments, we initialize the neural network parameters consistently: weights follow a standard Gaussian distribution while biases are set to zero vectors, all using an identical random seed. This ensures the same initializers across all test cases.

Sequential training protocol. Our training strategy follows a sequential two-phase approach. Initially, we optimize the encoder network to maximize accuracy on a test set of 500 samples (for either PoIs or observations). Subsequently, using this pre-trained encoder, we optimize the decoder network to achieve optimal accuracy on the same test dataset size. Our experimental investigations have demonstrated that simultaneous training of both encoder and decoder networks does not yield superior accuracy compared to this sequential approach. This can be attributed to two key factors: first, the decoder’s performance is primarily contingent on the quality of the encoder’s output; and second, the simultaneous optimization of both networks can compromise encoder accuracy due to the presence of the decoder loss term. Furthermore, the expanded parameter space in simultaneous training increases the likelihood of the optimizer converging to local minima. A theoretical discussion of the simultaneous training strategy compared to the sequential training strategy is presented in section 2.5. Therefore, we shall focus on the results obtained by the sequential training strategy.

3.1. 2D heat equation

We investigate the following heat equation:

$$\begin{aligned} -\nabla \cdot (e^u \nabla \omega) &= 20 & \text{in } \Omega = (0, 1)^2 \\ \omega &= 0 & \text{on } \Gamma^{\text{ext}} \\ \mathbf{n} \cdot (e^u \nabla \omega) &= 0 & \text{on } \Gamma^{\text{root}}, \end{aligned}$$

where u represents the (log) conductivity coefficient field (the parameter of interest PoI), ω denotes the temperature field, and \mathbf{n} is the unit outward normal vector along the Neumann boundary Γ^{root} . As illustrated in the left panel of fig. 2, we discretize the domain using a 16×16 grid, with 10 randomly distributed observation points sampling from the discretized field ω . We aim to achieve two primary goals: (1) learning an inverse mapping to directly reconstruct the conductivity coefficient field \mathbf{u} from 10 discrete observations $\mathbf{y} = B\omega$, and (2) learning a PtO map or forward map that predicts either the temperature observations \mathbf{y} or the temperature field ω given a conductivity coefficient field \mathbf{u} .

Generating train and test data sets. We start with drawing the parameter conductivity samples via a truncated Karhunen-Loève expansion

$$u(x) = \sum_{i=1}^q \sqrt{\lambda_i} \phi_i(x) \mathbf{u}_i, \quad x \in [0, 1]^2,$$

where (λ_i, ϕ_i) is the eigenpair of a two-point correlation function from [19], and $\mathbf{u} = \{\mathbf{u}_i\}_{i=1}^q \sim \mathcal{N}(0, I)$ is a standard Gaussian random vector. We choose $q = 15$ eigenvectors corresponding to the first 15 largest eigenvalues. For each sample \mathbf{u} we solve the heat equation for the corresponding temperature field ω by finite element method. The observation samples $\mathbf{y}^{\text{clean}}$ are constructed by extracting values of the temperature field ω at the 10 observable locations (see fig. 2), followed by the addition of Gaussian noise with the noise level of $\delta = 0.5\%$. Our training dataset consists of 100 independently drawn sample

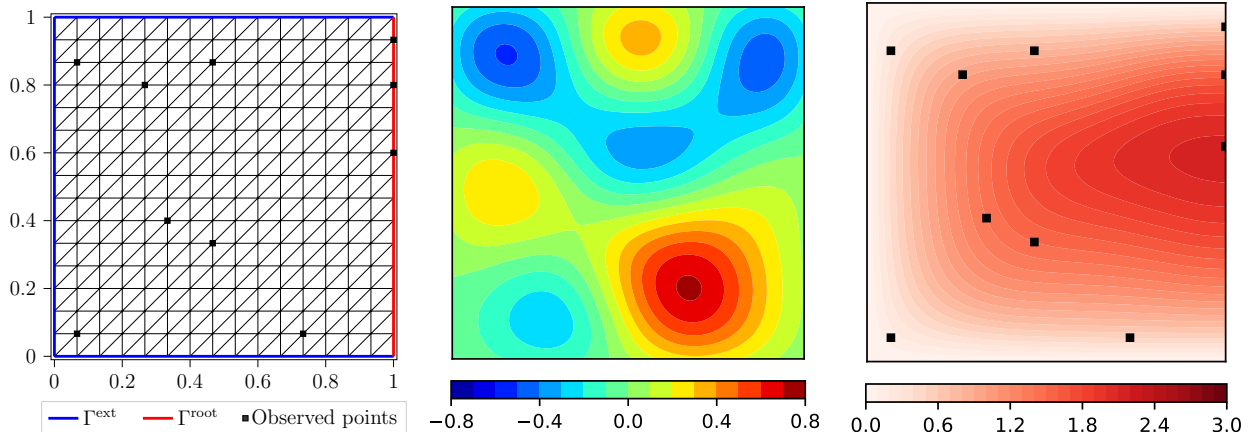


Figure 2: 2D heat equation. **Left:** Domain, boundary conditions, 16×16 finite element discretization mesh, and 10 random observation locations. **Middle:** A sample of the PoI (the heat conductivity field). **Right:** The corresponding state (temperature field), observations (temperatures) are taken at 10 observed points. This pair of PoI and observation sample is used for training in one training sample case.

Table 3: 2D heat equation. The average relative error for inverse solutions and forward solutions (observations) over 500 test samples obtained by all approaches trained with $\{1, 100\}$ training samples. The model-constrained approaches are more accurate for both inverse (comparable to the Tikhonov—Tik—approach) and forward solution, and within the model-constrained approaches, TAEN and TAEN-Full are the most accurate ones: in fact one training sample is sufficient for these two methods.

Approach	1 training sample		100 training samples	
	Inverse (%)	Forward	Inverse (%)	Forward
nPOP	100.18	3.99×10^{-1}	80.48	5.30×10^{-2}
nOPO	107.55	2.90×10^{-1}	50.18	1.09×10^{-1}
mcPOP	107.99	3.99×10^{-1}	87.60	5.30×10^{-2}
mcOPO	108.28	2.73×10^{-2}	46.32	3.94×10^{-4}
mcOPO-Full	108.28	4.21×10^{-2}	46.32	4.56×10^{-4}
TAEN	45.23	1.57×10^{-4}	45.03	1.22×10^{-4}
TAEN-Full	45.23	8.80×10^{-4}	45.03	2.12×10^{-4}
Tik	44.99		44.99	

pairs. The middle and right figures in fig. 2 show the conductivity coefficient fields u and its corresponding temperature field ω for the first pair out of 100 training sample pairs. This particular pair serves as the training data for the single-sample training case for all approaches. For the inference (testing) step, we generate 500 independently drawn pairs (\mathbf{u}, ω) following the same procedure discussed above.

Learned inverse and PtO/forward maps accuracy. We compare all approaches using the aforementioned two-phase sequential training protocol. All methods are imple-

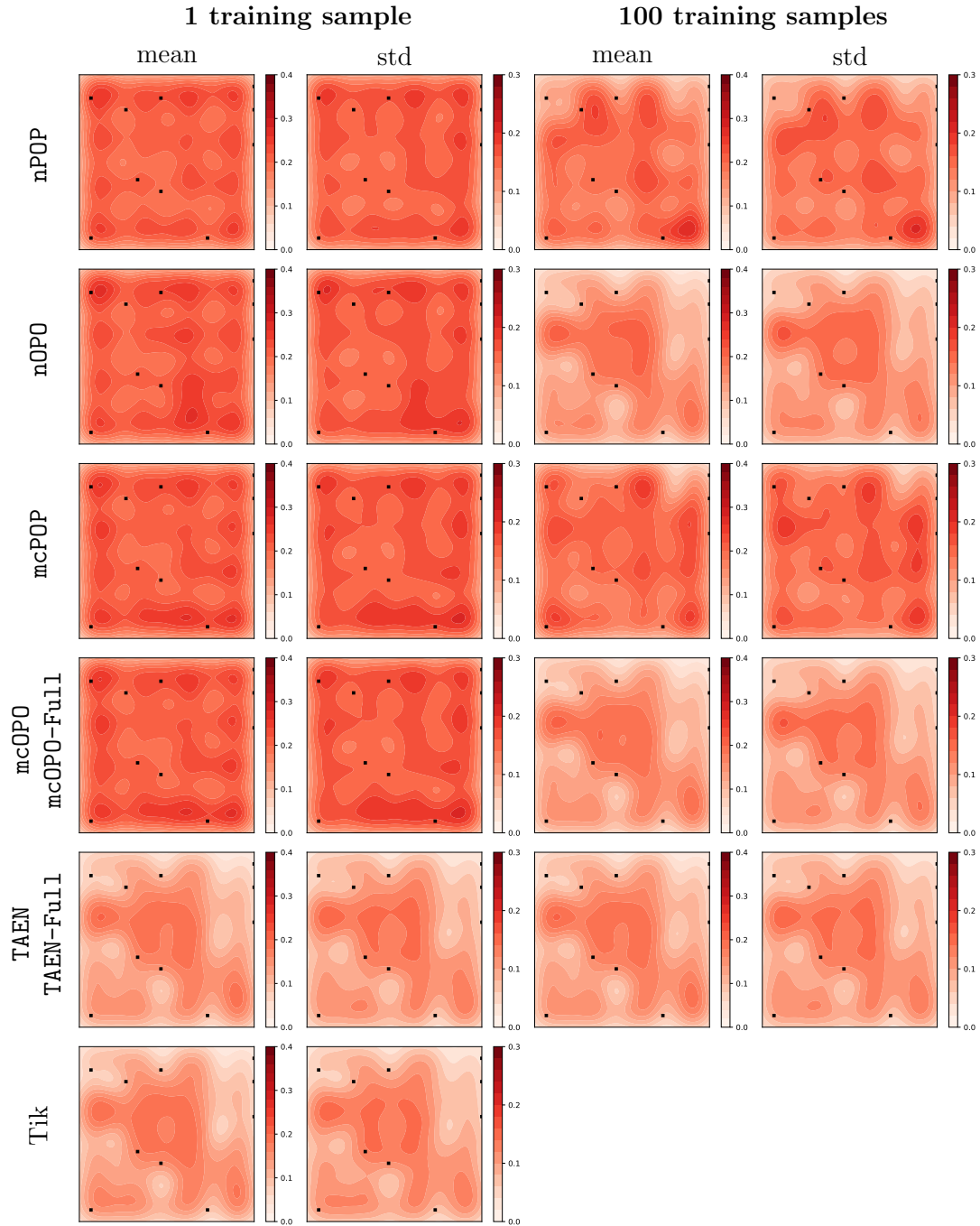


Figure 3: 2D heat equation. Mean and standard deviation of absolute error for 500 test inverse solutions obtained from different approaches. Black points are observational locations. Note that TAEN and TAEN-Full (and similarly for nPOP and mcPOP approaches) have the same encoder (that encodes the inverse solutions), their (identical) results are shown on the 5th row. Relatively to the Tikhonov approach (Tik), the model-constrained approaches are more accurate, and within the model-constrained approaches, TAEN and TAEN-Full are the most accurate ones: in fact one training sample is sufficient for these two methods.

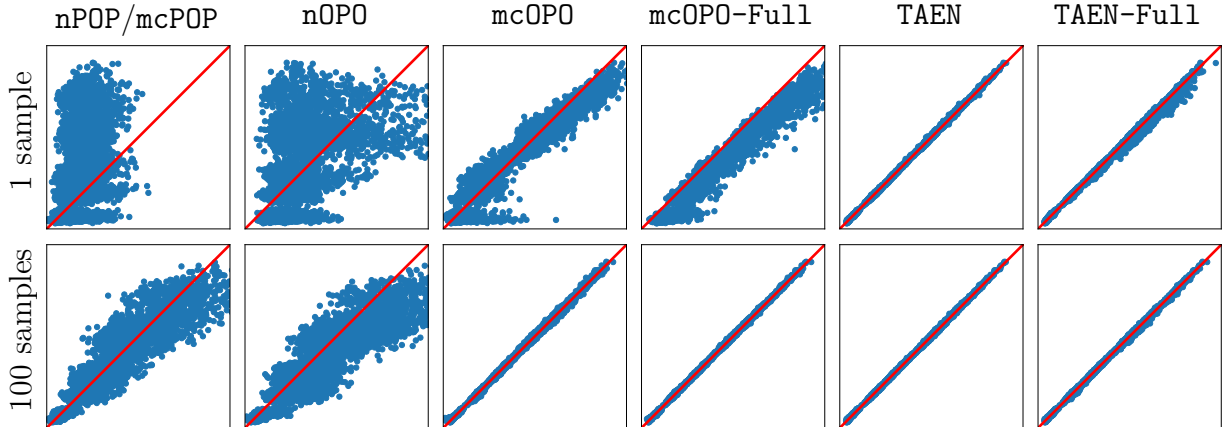


Figure 4: 2D heat equation. The comparison of 500 test predicted forward solution (at the observational locations) obtained from different approaches. In all plots plot, the x-axis is the magnitude of the true observation, and the y-axis is the magnitude of the predicted observation, both axes has range of $[0, 3]$. The red line indicates the perfect matching between predictions and truth observations. **Top row:** Trained with 1 training sample. **Bottom row:** Trained with 100 training samples. As can be seen, model-constrained approaches are more accurate, and within the model-constrained approaches, TAEN and TAEN-Full are the most accurate ones: in fact one training sample is sufficient for these two methods.

mented under two scenarios: training with a single training sample and training with 100 training samples. For mcOPO, mcOPO-Full, TAEN and TAEN-Full approaches, we perform data randomization for each epoch by adding random noise with magnitude $\varepsilon = 10\%$ to the already-noise-corrupted observation samples as specified in eq. (10). table 3 (with further details in fig. 3 and fig. 4, respectively) summarizes the average relative errors (with further details on average mean, standard deviation, and correlation between the true and predicted forward solutions, respectively) for 500 test samples calculated using eq. (12), for both inverse and predicted observable solutions. As can be seen, the model-constrained approaches are more accurate, and within the model-constrained approaches, TAEN and TAEN-Full are the most accurate ones: in fact one training sample is sufficient for these two methods.

Let us provide additional discussions on inverse learning (see table 3 and fig. 3). TAEN and TAEN-Full attain inverse solution accuracy of 45.23%, comparable to the traditional Tikhonov regularization method with 44.99% error. In contrast, all other methodologies (nPOP, nOPO, mcPOP, mcOPO, and mcOPO-Full) fail to produce meaningful results. This performance disparity is due to the superior generalization capability of the TAEN and TAEN-Full approaches, while other methods suffer from overfitting the provided training sample. As presented in section 2.4, TAEN and TAEN-Full integrated with data randomization technique allows learning the inverse map as good as the Tikhonov regularization framework for linear inverse problems with only one arbitrary observation training sample. The data randomization technique serves two crucial functions: Exploring the unseen test observation sample space and exploiting the underlying physics via the model-constrained

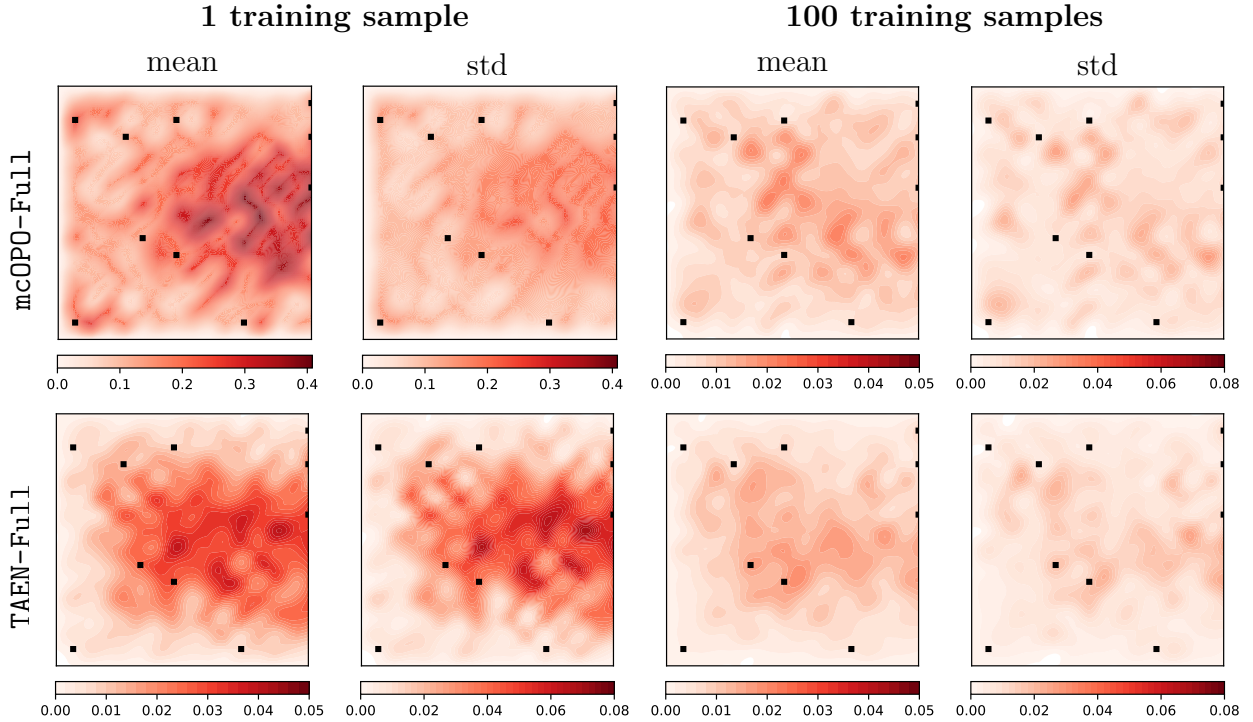


Figure 5: 2D heat equation. Mean and standard deviation of absolute pointwise error for 500 full state test solutions obtained from **TAEN-Full** and **mcOPO-Full**. Black dots are the observational locations. The former is more accurate, especially for the case with one training sample in which it achieves two orders of magnitude smaller error.

term.

Next, we provide further details on learning PtO/forward maps (see table 3 and fig. 4). **TAEN** and **TAEN-Full** can achieve highly accurate predictions of temperature solutions through the PtO/forward map (decoder), achieving relative errors of $1.57\text{e-}04$ and $8.80\text{e-}04$, respectively. This demonstrates their capability to learn accurately PtO/forward mappings from a single observation sample, again thanks to the data randomization. Since **TAEN** learns the observations directly, it is more accurate than **TAEN-Full** which aims to learn the full solution state. While our analysis in section 2.3.2 indicates that **mcOPO** and **mcOPO-Full** can theoretically learn exact PtO/forward maps in linear problems, their actual performance (errors of $2.73\text{e-}02$ and $4.21\text{e-}2$, respectively) falls short compared to **TAEN** and **TAEN-Full**. This underperformance can be attributed to two key factors: inaccurate inverse solutions obtained from the encoder and the nonlinear forward map. On the other hand, **nPOP**, **nOPO**, and **mcPOP** yield inaccurate PtO mappings, which is consistent with their purely data-driven architecture that does not encode physical constraints. The spatial distribution of prediction errors is further examined in fig. 5, which depicts the mean and standard deviation of absolute pointwise errors for 500 test temperature field samples (unseen full state solutions). It can be seen, **TAEN-Full** framework demonstrates consistently lower error statistics (two orders of magnitude smaller for one-sample case) compared to **mcOPO-Full**. These re-

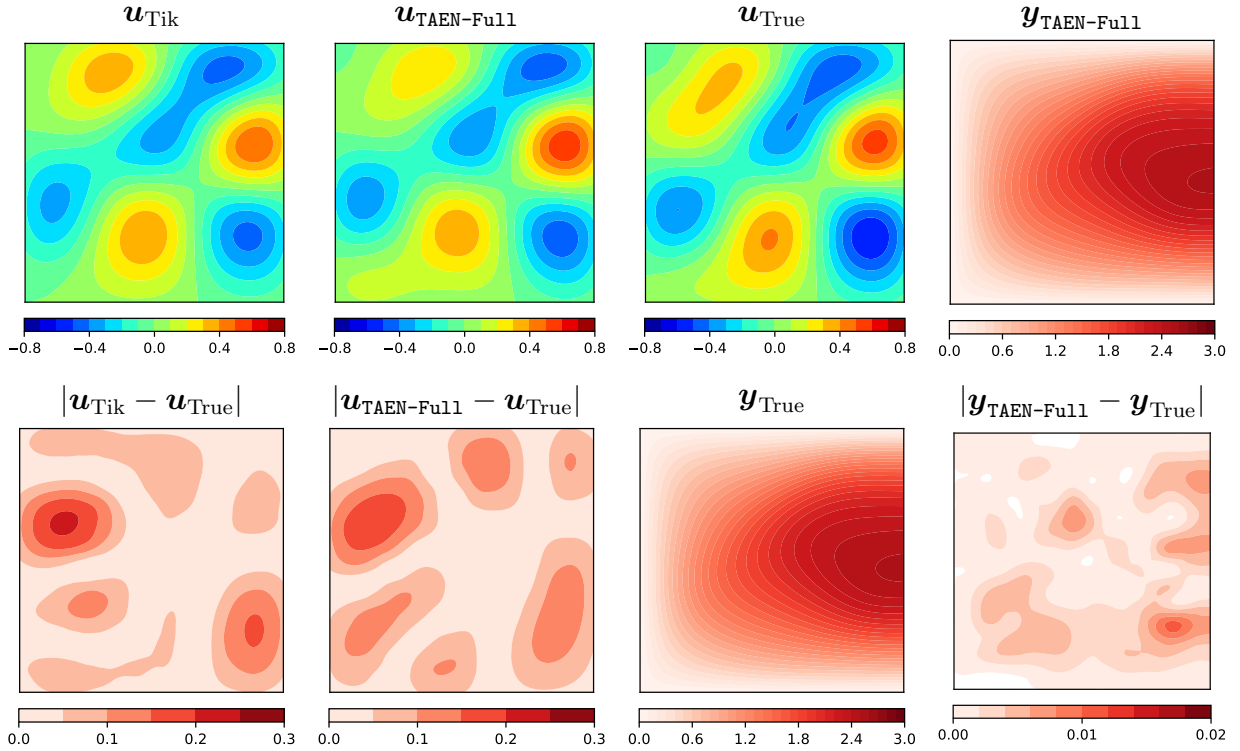


Figure 6: 2D heat equation. A (random) representative case of inverse and full forward solution obtained by TAEN-Full trained with 1 training sample coupled with data randomization of noise level $\sigma = 0.1$. TAEN-Full inverse solution is comparable to the Tikhonov (Tik) inverse counterpart, and both are consistent with the ground truth (True). TAEN-Full full forward solution is almost identical (in fact within 3 digits of accuracy) to the underlying true solution.

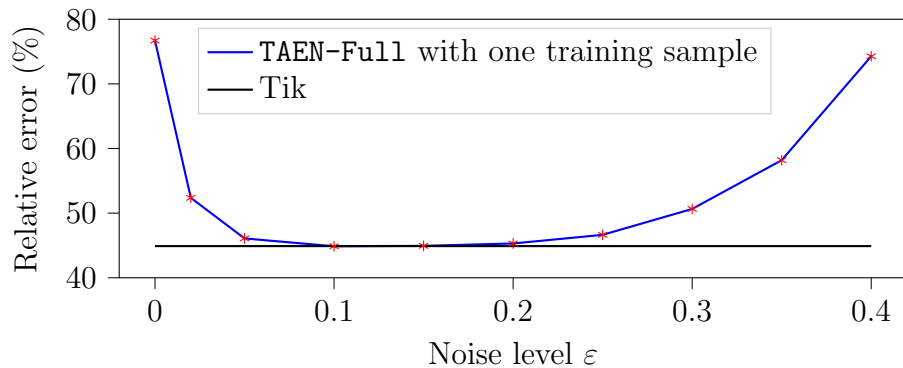


Figure 7: 2D heat equation. Relative error of inverse solution over 500 test samples with different noise levels.

sults provide additional validation of the TAEN-Full framework's efficacy in learning forward mappings (in tandem with learning the inverse solutions).

We have also seen that, for the larger data set of 100 samples, the accuracy of for-

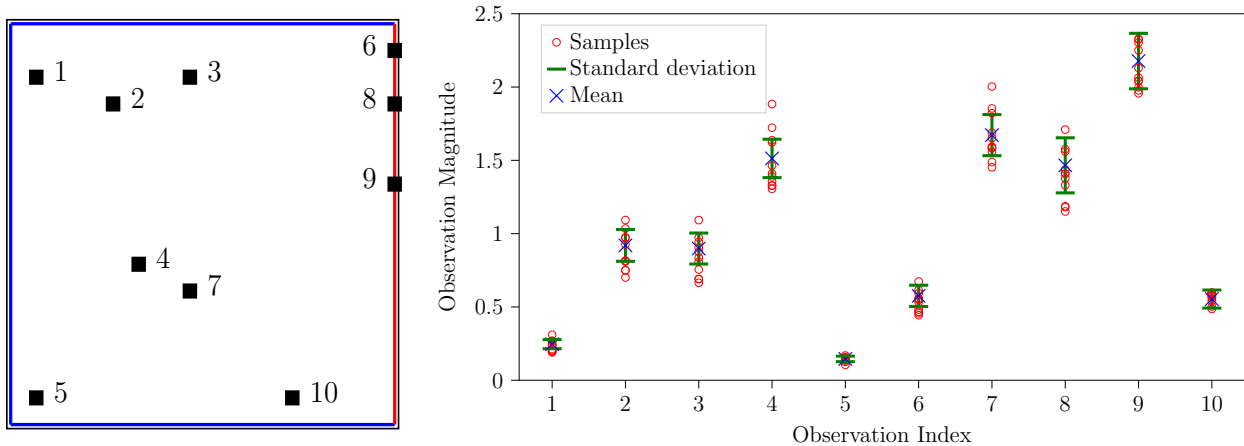


Figure 8: 2D heat equation. **Left:** Index of 10 observational locations. **Right:** Mean and standard deviation of observation magnitudes of 10000 true observation samples at the observational locations. The magnitudes of the predicted solutions of 10 different observation samples for single-sample training cases.

ward and inverse maps for all approaches is improved as expected. TAEN and TAEN-Full maintain their superior performance for both PtO/forward and inverse solutions. We emphasize that the best inverse map obtained from TAEN and TAEN-Full is just as good as the Tikhonov regularization method; thus, not much improvement is observed compared to the single-sample training case. In other words, **one training data is sufficient for TAEN and TAEN-Full**. Coming in second are mcOP0 and mcOP0-Full. Unlike the single-sample training scenario, these approaches now achieve reliable inverse maps (encoders), enabling their model-constrained decoders to achieve high accuracy in PtO/forward solutions. Meanwhile, the purely data-driven approach nOP0, without additional information provided by the physics constraints, produces lower accuracy in inverse solutions compared to mcOP0. This is not surprising, as analyzed in section 2.2.2, the inaccurate inverse solutions from its encoder network inevitably lead to poor PtO solutions, resulting in its least accuracy. On the other hand, the nPOP and mcPOP approaches, which prioritize learning the PtO map (encoder), achieve better PtO solution accuracy than nOP0. Consequently, the inaccuracy of encoder outputs (due to the nonlinear PtO map) propagates through the decoder, resulting in the least accurate inverse solutions, even with the forward solver as the physics constraint.

fig. 6 shows a (random) representative inverse (conductivity field) and full state (temperature field) forward solutions obtained by TAEN-Full trained with one training sample coupled with data randomization of noise level $\varepsilon = 10\%$. It can be seen that the inverted conductivity field exhibits accuracy comparable to the Tikhonov regularization solution, and both closely approximate the true conductivity field distribution. Furthermore, the predicted temperature field demonstrates excellent agreement with the ground truth solution. These results underscore the effectiveness of combining model-constrained learning with data randomization techniques in the TAEN-Full framework. We would like to point

out that the significant difference in the test case in fig. 6 and the training sample in fig. 2 demonstrates the framework’s robust generalization capabilities to completely different test samples. This desirable characteristic enables the development of inverse and forward surrogate models using minimal training data—namely one single training sample without ground truth PoI—while maintaining reliable performance on unseen test cases. We would like to point out that such a capability comes with an offline cost: differentiable forward solver is required in this paper. One remedy is to train a surrogate (e.g. neural network) for the forward map or to use a differentiable reliable surrogate if available.

TAEN-Full robustness to a wide range of noise levels. We further investigate the robustness of TAEN-Full across varying noise levels using a single training sample. fig. 7 demonstrates that TAEN-Full achieves relative errors comparable to the Tikhonov regularization framework across a broad noise spectrum (8% to 20%) for 500 test inverse solutions. Outside this “optimal range”, TAEN-Full does not yield acceptable accuracy. On the one hand, with low noise levels, the data randomization technique insufficiently explores the space of potentially unseen test samples, limiting generalization capabilities. On the other hand, excessive noise levels result in overwhelmingly corrupted samples that are statistically indistinguishable, and thus degrading the accuracy of the learned surrogate models. These observations are consistent with the theoretical prediction in section 2.6. We would like to point out that the minimum relative error achieved by TAEN-Full matches that of the Tikhonov regularization framework, indicating that, as designed, TAEN-Full successfully learns the Tikhonov regularization solver using only a single training sample without requiring ground truth PoI data.

TAEN-Full robustness to arbitrary single-sample. In this section, we investigate the robustness of the TAEN-Full framework to one arbitrarily chosen sample for training. To that end, ten independent training instances are conducted, each utilizing a single sample randomly selected from a pool of 100 training samples. The left figure in fig. 8 presents the spatial distribution of 10 observational points, including their location indices. The right figure of fig. 8 shows the statistical characteristics (mean and standard deviation) of 10000 distinct observation samples, and the observation magnitudes for the 10 randomly selected training cases at their respective locations. Statistical analysis of the TAEN-Full performance across these 10 distinct training instances yields an average relative error of 45.32% (again similar to the Tikhonov regularization error) with a standard deviation of 0.32% for inverse solutions. This small variance in relative error metrics demonstrates the TAEN-Full robustness with respect to an arbitrary individual sample in the single-sample training scenario. In particular, the result shows that the prediction error is similar for any of these 10 individual random samples when used in the TAEN-Full as the only training sample.

3.2. Navier-Stokes equations

The vorticity form of 2D Navier–Stokes equation for viscous and incompressible fluid [50] is written as

$$\begin{aligned}\partial_t \omega(x, t) + v(x, t) \cdot \nabla \omega(x, t) &= \nu \Delta \omega(x, t) + f(x), & x \in (0, 1)^2, t \in (0, T], \\ \nabla \cdot v(x, t) &= 0, & x \in (0, 1)^2, t \in (0, T], \\ \omega(x, 0) &= u(x), & x \in (0, 1)^2,\end{aligned}$$

where $v \in (0, 1)^2 \times (0, T]$ denotes the velocity field, $\omega = \nabla \times v$ represents the vorticity, and u defines the initial vorticity which is the parameter of interest. The forcing function is specified as $f(x) = 0.1(\sin(2\pi(x_1 + x_2)) + \cos(2\pi(x_1 + x_2)))$, with viscosity coefficient $\nu = 10^{-3}$. The computational domain is discretized using a uniform 32×32 mesh in space, while the temporal domain $t \in (0, 10]$ is partitioned into 1000 uniform time steps with $\Delta t = 10^{-2}$. The inverse problem aims to reconstruct the initial vorticity field u from vorticity measurements \mathbf{y} collected at 20 random spatial locations from the vorticity field ω at the final time $T = 10$.

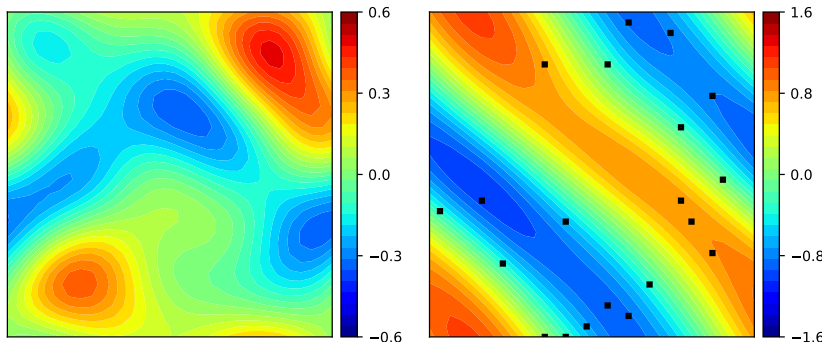


Figure 9: 2D Navier–Stokes equation. Left: A sample of the PoI u . **Right:** A corresponding vorticity field ω at final time $T = 10$, observation \mathbf{y} are extracted at 20 random observed points. This pair of PoI and observation/vorticity field is used for training in one training sample case.

Generating train and test data sets. To generate data pairs of (u, ω) , we draw samples of $u(x)$ using the truncated Karhunen-Loève expansion

$$u(x) = \sum_{i=1}^{24} \sqrt{\lambda_i} \phi_i(x) z_i,$$

where $z_i \sim \mathcal{N}(0, 1)$, $i = 1, \dots, 24$, and (λ_i, ϕ_i) are eigenpairs obtained by the eigendecomposition of the covariance operator $7^{\frac{3}{2}}(-\Delta + 49\mathbf{I})^{-2.5}$ with periodic boundary conditions. Next, we discretize the initial vorticity $u(x)$, denoted as \mathbf{u} , and we solve the Navier-Stokes equation by the stream-function formulation with a pseudospectral method [50] to obtain a discrete representation $\boldsymbol{\omega}$ of $\omega(x, t)$ at time $t = 10$. The observation data \mathbf{y} consists of the vorticity field $\boldsymbol{\omega}$ at $T = 10$ at 20 randomly distributed observational locations, with

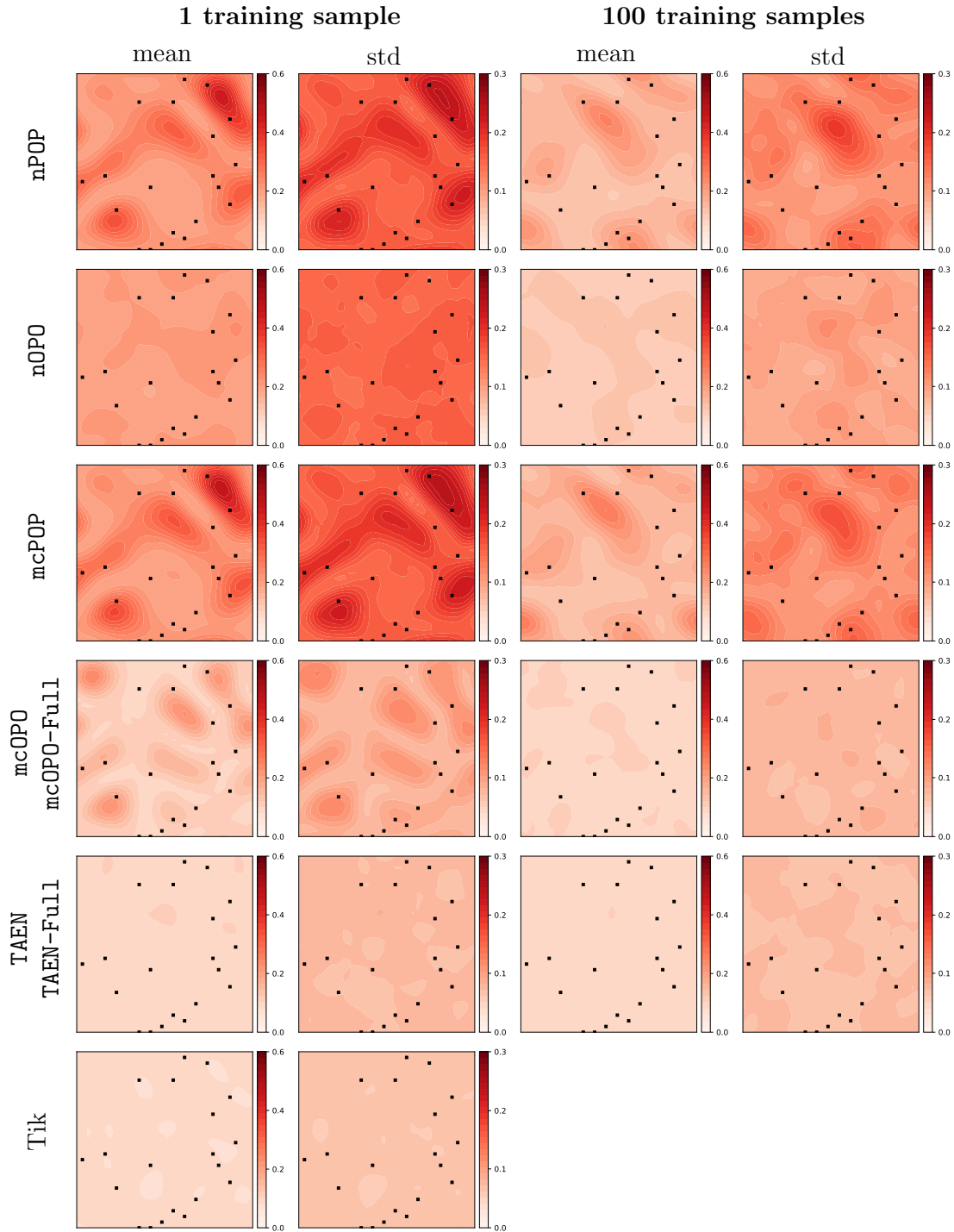


Figure 10: 2D Navier–Stokes equation. Mean and standard deviation of absolute error of 500 test inverse solutions obtained from different approaches. Black points are observation locations. Relatively to the Tikhonov approach (Tik), the model-constrained approaches are more accurate, and within the model-constrained approaches, TAEN and TAEN-Full are the most accurate ones: in fact one training sample is sufficient for these two methods.

Table 4: 2D Navier–Stokes equation. Average relative error for inverse solutions and PtO/forward solutions obtained by all approaches trained with $\{1,100\}$ training samples. The model-constrained approaches are more accurate for both inverse (comparable to the Tikhonov—Tik—approach) and forward solution, and within the model-constrained approaches, TAEN and TAEN-Full are the most accurate ones: in fact one training sample is sufficient for these two methods.

Approach	1 training sample		100 training samples	
	Inverse (%)	Forward	Inverse (%)	Forward
nPOP	156.99	2.99×10^{-1}	72.22	6.72×10^{-2}
nOPO	103.94	5.60	40.20	5.94×10^{-1}
mcPOP	161.48	2.99×10^{-1}	76.33	6.72×10^{-2}
mcOPO	46.43	5.15×10^{-1}	27.29	2.20×10^{-3}
mcOPO-Full	46.43	3.79×10^{-1}	27.29	2.12×10^{-3}
TAEN	25.68	2.14×10^{-3}	24.54	1.49×10^{-3}
TAEN-Full	25.68	2.10×10^{-3}	24.54	1.45×10^{-3}
Tik	22.71		22.71	

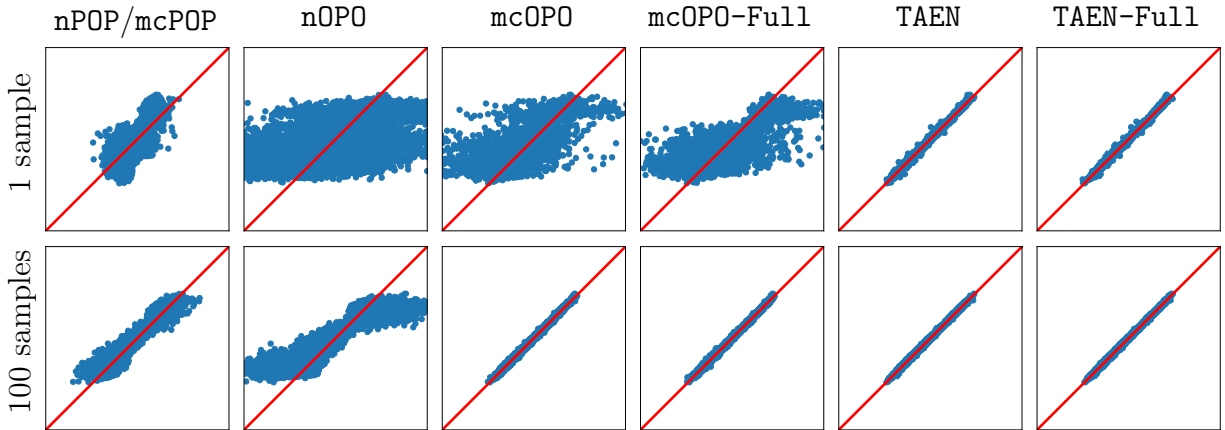


Figure 11: 2D Navier–Stokes equation. The comparison of the predicted observations on 500 test samples. In all plots plot, the x-axis is the magnitude of the true observation, and the y-axis is the magnitude of the predicted observation, both axes have a range of $[-3, 3]$. The red line indicates the perfect matching between predictions and the ground truth observation data set. **Top row:** Trained with 1 training sample. **Bottom row:** Trained with 100 training samples. As can be seen, model-constrained approaches are more accurate, and within the model-constrained approaches, TAEN and TAEN-Full are the most accurate ones: in fact one training sample is sufficient for these two methods.

the subsequent addition of $\delta = 2\%$ Gaussian noise. Two distinct datasets are generated: a training set comprising 100 independent samples and a test set containing 500 samples. fig. 9 illustrates the first sample pair from the training dataset of 100 samples, which serves as the training sample for single-sample training scenarios for all approaches.

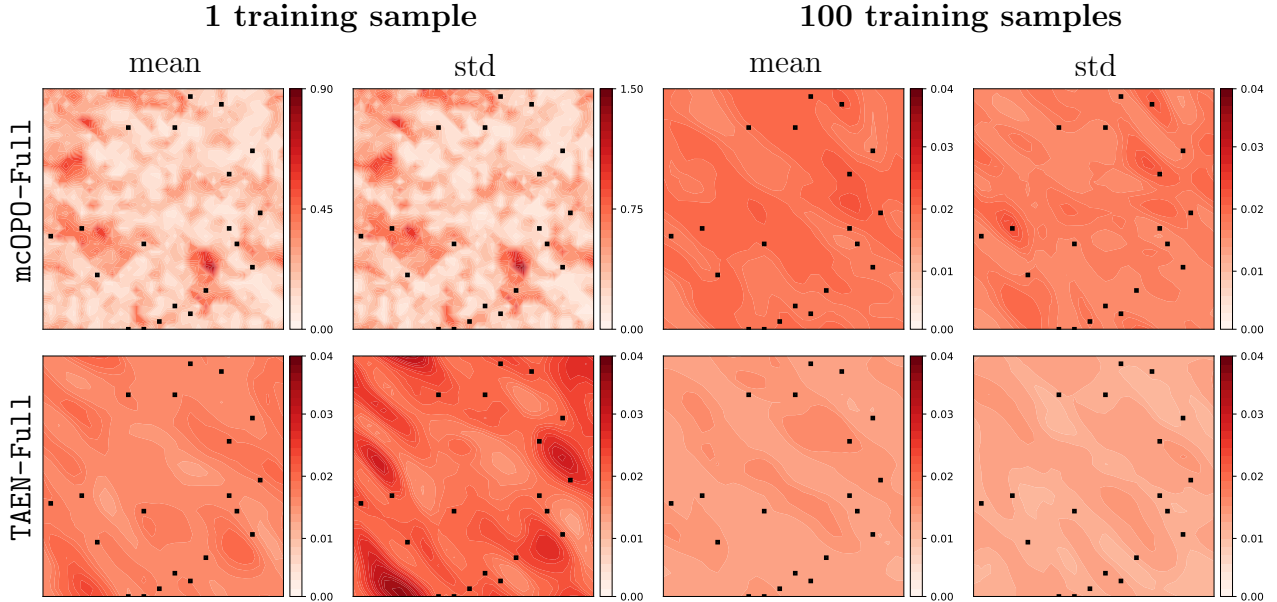


Figure 12: 2D Navier–Stokes equation. Mean and standard deviation of absolute pointwise error for 500 test vorticity solutions at $T = 10$ obtained from mcOPO-Full and TAEN-Full. Black points are observational locations. TAEN-Full is more accurate, especially for the case with one training sample in which it achieves two orders of magnitude smaller error.

Learned inverse and PtO/forward maps accuracy. Following the same procedure used for the 2D Poisson equation, encoder, and decoder networks are trained sequentially for two cases: using a single training sample pair (shown in fig. 9) and using 100 training sample pairs. For mcOPO, mcOPO-Full, TAEN and TAEN-Full approaches, randomization are performed at each epoch with noise level $\varepsilon = 25\%$. table 4 presents the average relative errors of inverse and PtO/forward solutions computed from 500 test samples for all approaches.

When trained on a single sample, TAEN and TAEN-Full achieve the lowest average relative error of 25.68% (closest to the gold-standard Tikhonov regularization solution with 22.71% error) for inverse solutions among all approaches. Similarly, their PtO/forward solutions demonstrate superior accuracy with average relative errors of 2.14×10^{-3} and 2.10×10^{-3} , respectively. This generalization accuracy is owing to the combination of data randomization and forward solver model-constrained terms. The mcOPO and mcOPO-Full approaches come in second with regarding to the accuracy for inverse solutions, with a relative error of 46.43%. This reduced accuracy (relatively to TAEN and TAEN-Full) stems from a strong bias toward the single training sample, despite the forward solver constraint, as predicted in section 2.3.2. mcPOP, nOPO, and nPOP exhibit significantly higher average relative errors of 161.48%, 103.94%, and 156.99% respectively for inverse solutions. These poor results are expected for nOPO and nPOP due to their purely data-driven nature, thus limiting generalization. For mcPOP, the inaccurate encoder (learned PtO map) propagates errors to the decoder training, resulting in imprecise inverse surrogate models. For PtO/forward solutions, nPOP, nOPO, mcPOP, mcOPO, and mcOPO-Full fail to produce accurate surrogate models, again due

to overfitting to the single training sample despite forward solver regularization.

When we increase the number of training samples to 100, and thus providing more information about the problem under consideration, significant accuracy improvements are observed for all approaches for both inverse and PtO/forward surrogate models. **TAEN** and **TAEN-Full** approaches maintain the best performance, achieving average relative errors of 24.54% for inverse solutions compared to the Tikhonov (Tik) method with of 22.71%. Their PtO/forward solutions exhibit good accuracy with average relative errors of 1.49×10^{-3} and 1.45×10^{-3} , respectively. The average relative error of the inverse solution obtained by **mcOPO** and **mcOPO-Full** is 27.29%, which is the second best among all approaches. The relative error of the PtO/forward solution obtained by **mcOPO** and **mcOPO-Full** is 2.20×10^{-3} and 2.12×10^{-3} , respectively, which is almost as good as **TAEN** and **TAEN-Full**. This indicates the roles of model-constrained terms in reducing the overfitting effect when sufficient training data is provided. In contrast, **nPOP** and **mcPOP** show substantially higher relative errors of 72.22% and 76.33%, respectively, for inverse solutions. These high errors stem from inaccuracies in their pre-trained PtO map (encoder), consistent with observations from the single-sample training scenario. Meanwhile, **nOPO** framework shows improved inverse solution accuracy with a relative error of 40.20%, yet remains less accurate than the model-constrained approaches (**mcOPO**, **mcOPO-Full**, **TAEN**, and **TAEN-Full**). This reduced performance is consistent with the error analysis for linear problems in section 2.3. Moreover, **nOPO**'s PtO solution accuracy remains notably poor (5.94×10^{-1}) despite the richer training dataset with 100 data pairs, reflecting the inherent PtO mapping errors analyzed in section 2.2.2.

We further elaborate on the accuracy of forward and inverse surrogate models obtained from all approaches. fig. 10 illustrates the spatial distribution of error statistics, presenting both mean and standard deviation of the absolute errors between predicted and ground truth inverse solutions for 500 test cases. **TAEN** and **TAEN-Full** frameworks demonstrate superior performance, exhibiting the lowest mean and standard deviation of absolute errors across the domain for both single-sample and 100-sample training scenarios. The **mcOPO** and **mcOPO-Full** approaches achieve comparable accuracy only when trained with 100 samples, while their single-sample training results show substantially high mean and standard deviation absolute error values. This performance difference underscores the enhanced generalization capabilities of the **TAEN** and **TAEN-Full** frameworks compared to their model-constrained counterparts, **mcOPO** and **mcOPO-Full**. In contrast, the **mcPOP**, **nPOP**, and **nOPO** approaches consistently demonstrate significantly higher mean and standard deviation of absolute errors across the domain in both training scenarios.

fig. 11 presents a quantitative comparison between predicted observations and ground truth observations for different approaches. In the single-sample training scenario, only **TAEN** and **TAEN-Full** demonstrate accurate predictions, while other approaches exhibit substantial deviations from ground truth values. With the 100-sample training dataset, **mcOPO** and **mcOPO-Full** join **TAEN** and **TAEN-Full** in achieving significant improvements in observation and vorticity field predictions. However, **nPOP**, **nOPO**, and **mcPOP** continue to produce inaccurate predictions even with 100 training data. The capability of **TAEN-Full** and **mcOPO-Full** to function as direct surrogate solvers for the Navier-Stokes equation deserves particular at-

tention. fig. 12 illustrates the spatial distribution of error statistics, showing the mean and standard deviation of absolute pointwise errors between predicted and true vorticity fields across 500 test samples. In the single-sample training scenario, mcOPO-Full exhibits high prediction errors, while TAEN-Full maintains good accuracy in vorticity field predictions (in fact two orders of magnitude smaller). The transition to 100-sample training yields marked accuracy improvements for both frameworks in vorticity field predictions, demonstrating their potential as efficient surrogate forward solvers when provided with sufficient training data.

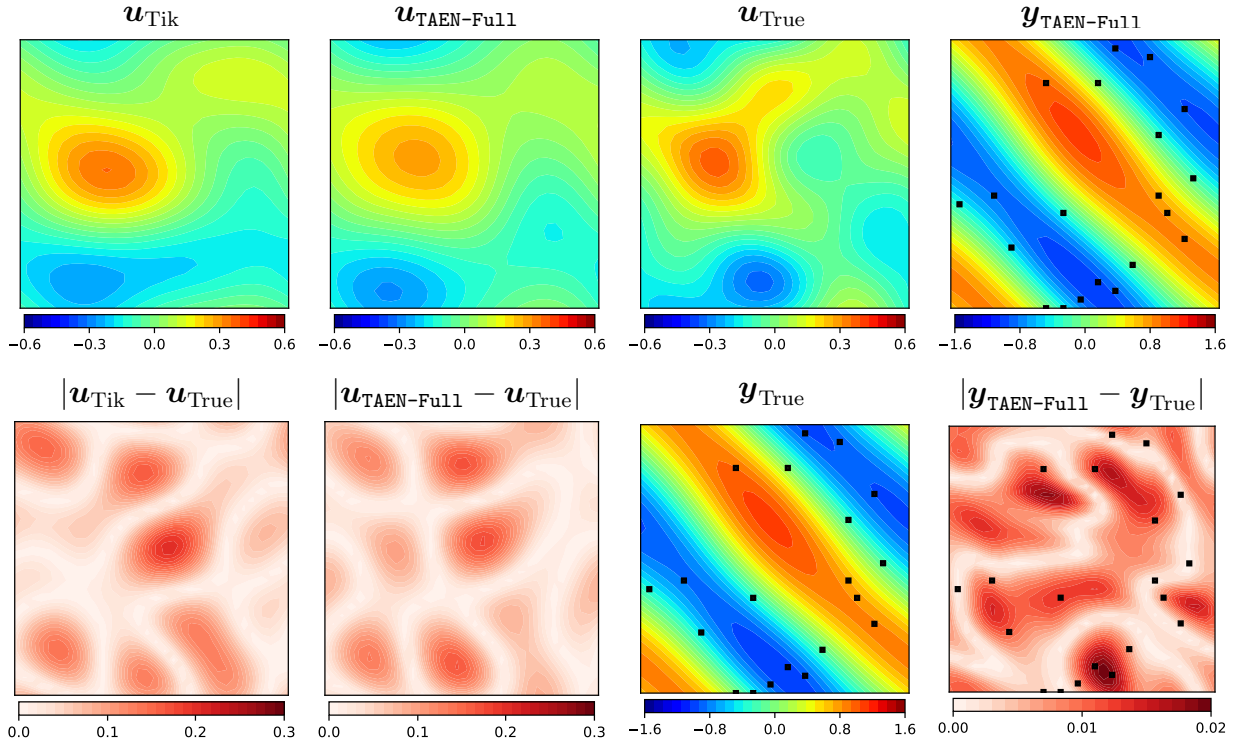


Figure 13: 2D Navier–Stokes equation. A (random) representative case of inverse and full forward solution at $T = 10$ obtained by TAEN-Full trained with 1 training sample coupled with data randomization of noise level $\sigma = 0.25$. TAEN-Full inverse solution is comparable to the Tikhonov (Tik) inverse counterpart, and both are consistent with the ground truth (True). TAEN-Full full forward solution is almost identical (in fact within 2 digits of accuracy) to the underlying true solution.

fig. 13 shows a (random) representative inverse (initial vorticity field) and full state (vorticity field) forward solutions obtained by TAEN-Full at $T = 10$ trained with one training sample coupled with data randomization of noise level $\varepsilon = 25\%$. It can be seen that the inverted initial vorticity field exhibits accuracy comparable to the Tikhonov regularization solution, and both closely approximate the true initial vorticity field. Furthermore, the predicted vorticity field at the final time demonstrates excellent agreement with the ground truth solution. These results underscore the effectiveness of combining model-constrained

learning with data randomization techniques in the TAEN-Full framework. It is important to note that the single training data pair, as shown in fig. 9, is completely different from the shown test sample under consideration. This observation demonstrates a generalization capacity of TAEN-Full framework to unseen test samples.

TAEN-Full robustness to a wide range of noise levels. A survey of TAEN-Full trained with one training sample over a wide range of noise levels is shown in fig. 14. As can be seen, the solution accuracy is robust for a wide range of noise from $\varepsilon \in [0.15, 0.5]$. Performance degradation is observed outside of this “optimal” noise level range. At low noise levels, the data randomization process provides insufficient variation to effectively explore the space of unseen test samples, limiting the framework’s ability to leverage forward solver constraints. On the other hand, excessive noise levels result in training data becoming statistically indistinguishable, degrading the framework’s capacity to learn accurate inverse mappings. These observations are consistent with the theoretical prediction in section 2.6.

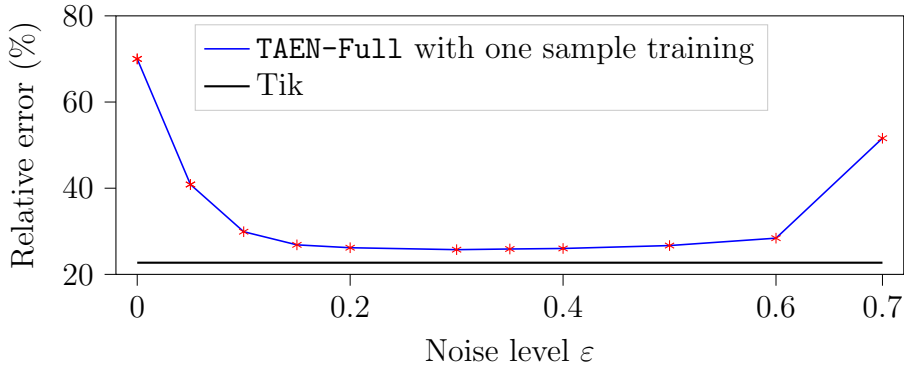


Figure 14: 2D Navier–Stokes equation. Relative error of inverse solution over 500 test samples with different noise levels.

TAEN-Full robustness to arbitrary single-sample. The robustness of TAEN-Full to an arbitrary one-training sample is examined. To be more specific, we randomly pick 12 samples out of 100 training sample data sets. The indices of 20 random observation locations are presented in the left figure in fig. 15. Meanwhile, the mean and standard deviation of observation magnitudes of 10000 true observation samples at corresponding 20 random observation locations and the predicted observation magnitudes from 12 different observation samples are shown in fig. 15. From 12 corresponding single-sample training cases, we obtain the mean and standard deviation of the relative error of the inverse solution is $25.88 \pm 0.19\%$ (again close to the Tikhonov regularization error). This small variance in relative error metrics demonstrates the TAEN-Full robustness with respect to an arbitrary individual sample in the single-sample training scenario. In particular, the result shows that the prediction error is similar for any of these 10 individual random samples when used in the TAEN-Full as the only training sample.

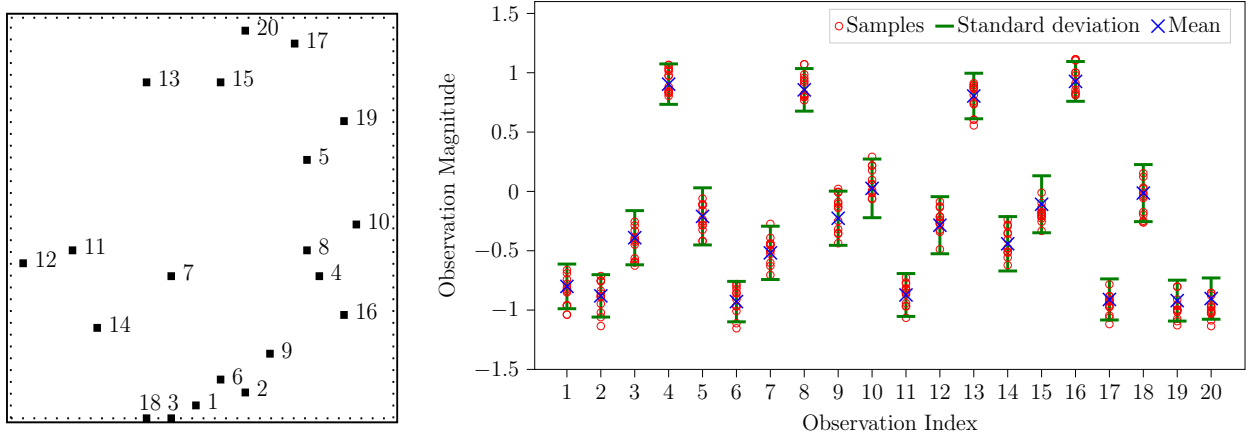


Figure 15: 2D Navier–Stokes equation. Left: Index of 20 observational locations. **Right:** Mean and standard deviation of observation magnitudes of 10000 true observation samples at observational locations. The observation magnitudes of 12 different single-sample training cases.

Table 5: The training cost (measured in hours) for the case of $n_t = 100$ randomized training samples for the heat and Navier–Stokes equations. The computational time (measured in seconds) for forward and inverse solutions using TAEN–Full and numerical solvers, and the speed-up of TAEN–Full (the fourth row) relative to numerical solvers using NVIDIA A100 GPUs on Lonestar6 at the Texas Advanced Computing Center (TACC).

		Heat equation	Navier–Stokes
Training Encoder + Training Decoder (hours)		2	16
Test/Inference (second)	Inverse (Encoder)	2.74×10^{-4}	2.93×10^{-4}
	Forward (Decoder)	2.86×10^{-4}	3.06×10^{-4}
Numerical solvers (second)	Inverse (Tikhonov)	4.36×10^{-2}	7.26
	Forward	3.01×10^{-2}	0.38
Speed up	Inverse	159	24,785
	Forward	105	1,241

3.3. Training cost and speedup with deep learning solutions

The training costs for the case of $n_t = 100$ randomized training samples for heat equation and Navier–Stokes equations are presented in Table 5. It can be observed that the heat equation requires a small amount of training time, about 2 hours, while the corresponding time for the Navier–Stokes equations is about 16 hours. It should be noted that executing the forward map and the backpropagation constitutes the majority of the training cost. Table 5 also provides information on the computational cost of reconstructing PoIs given an unseen test observation sample and solving for PDE solutions given an unseen PoI sample. Specifically, for inverse solutions, we use the classical Tikhonov (TIK) regularization technique and our proposed deep learning approach TAEN–Full using the encoder network. In contrast, we

use numerical methods and `TAEN-Full` decoder for predicting (forward) PDEs solutions. It can be seen that the training, and test computational time depends on the complexity of problems. We note that the complexity is estimated based on the number of time steps, the operations carried out per time step, and the mesh size. As can be seen, the more complicated the problem is, the more time Tikhonov and forward numerical solvers take to obtain the inverse and forward solutions, respectively. Unlike the Tikhonov approach, regardless of the complexity of the problems, the learned `TAEN-Full` encoder and decoder maps using one hidden layer with 5000 neurons takes the same small amount of time: approximately 0.0003 seconds. Note that the Tikhonov solver is implemented directly in `JAX` using the default BFGS algorithm with the gradient computed by the default Autograd functionality. Thus, the Tikhonov computation enjoys `JAX` optimized features including XLA (accelerated linear algebra), JIT (just-in-time compilation), and the nested primitive loop technique. In the meantime, the majority of computational time for numerical forward solvers stems from JIT compiling the numerical solvers. JIT functionality takes a significant amount of time to cache the modular function for the first, then all following calls of the same function are significantly faster. This is why, for simple problems such as the Heat equation, we observe a little difference between the forward solver and the Tikhonov solver which requires numerous forward solvers. Even with such optimization, numerical forward and Tikhonov solvers are still orders of magnitude slower than `TAEN-Full` neural networks. In particular, for the Navier-Stokes equation, `TAEN-Full` is 24,785 times faster than Tikhonov and 1,241 times faster than the numerical forward solver using the spectral method. We expect the computational gain to be more significant for larger-scale 3D time-dependent nonlinear forward problems. Clearly, once trained, obtaining `TAEN-Full` solutions is simply a feed-forward neural network evaluation, which could be close to real-time or real-time depending on the network’s depth and the width.

4. Conclusion

This paper presents a model-constrained Tikhonov autoencoder neural network framework, called `TAEN`, for solving forward and inverse problems simultaneously. A comprehensive error estimation analysis across pure data-driven, model-constrained, and Tikhonov model-constrained approaches is provided for linear problems. Moreover, among approaches, `TAEN` and its variant `TAEN-Full` uniquely achieve both the exact Tikhonov solver and exact PtO map/forward map using an arbitrary observation sample for linear problems. This beauty stems from incorporating the data randomization strategy with a proper noise level within the model-constrained framework. Additionally, we establish theoretical support for sequential encoder-decoder training over simultaneous optimization. Numerical experiments on 2D heat equation and 2D Navier-Stokes equations validate these theoretical findings, demonstrating that `TAEN` and `TAEN-Full` solutions achieve accuracy comparable to Tikhonov solutions for inverse problems and numerical forward solver solutions for forward problems while delivering computational speedups of several orders of magnitude, using only one arbitrary training sample. The numerical results also shown that `TAEN` and `TAEN-Full` are robust, in the sense that their performance does not vary, for a wide range on noise level

and the arbitrarily of the single training sample. Ongoing work focuses on extending the TAEN framework to variable observational locations for inverse problems, where we anticipate developing encoders adaptable to diverse observation scenarios (varying measurement locations and quantities) while maintaining accurate PtO map/forward map representation through the decoder. Future work includes extensions to statistical inversions. While TAEN’s primary limitation, namely the requirement for a differentiable solver during training, can be addressed through differential numerical libraries or by substituting differential residual evaluation for the differentiable solver, these developments will be detailed in subsequent publications.

Acknowledgments

This research is partially funded by the National Science Foundation awards NSF-OAC-2212442, NSF-2108320, NSF-1808576, and NSF-CAREER-1845799; by the Department of Energy award DE-SC0018147 and DE-SC0022211. The authors would like to thank Arjit Seth, Krishnanunni Chandradath Girija, and Wesley Lao for fruitful discussions. The authors also acknowledge the Texas Advanced Computing Center (TACC) at The University of Texas at Austin for providing HPC, visualization, database, or grid resources that have contributed to the research results reported within this paper. URL: <http://www.tacc.utexas.edu>

5. Appendix

5.1. Derivation of $W_e, \mathbf{b}_e, W_d, \mathbf{b}_d$ for *nOPD*

We train the encoder and decoder sequentially. First, we train the encoder, given training data samples. Then, we train the decoder, given the pretrained encoder. The optimal solutions for this training strategy are derived as follows. The loss function for the encoder is given as:

$$\mathcal{L}_e = \frac{1}{2} \|W_e Y + \mathbf{b}_e \mathbf{1}^T - U\|_F^2$$

For simplicity, let’s denote $Z = W_e Y + \mathbf{b}_e \mathbf{1}^T$. Then, loss function for the decoder given a pre-trained encoder is

$$\mathcal{L}_d = \frac{1}{2} \|W_d Z + \mathbf{b}_d \mathbf{1}^T - Y\|_F^2$$

To find the optimal values, we set all gradients to zero and solve the resulting system of equations:

- Gradient with respect to \mathbf{b}_e

$$\frac{\partial \mathcal{L}_e}{\partial \mathbf{b}_e} = (W_e Y + \mathbf{b}_e \mathbf{1}^T - U) \mathbf{1} = (W_e Y + \mathbf{b}_e \mathbf{1}^T) \mathbf{1} - U \mathbf{1} = 0$$

Solving for \mathbf{b}_e we have:

$$\mathbf{b}_e = \frac{1}{n_t}(U\mathbf{1} - W_e Y \mathbf{1}) \quad (13)$$

- Gradient with respect to W_e

$$\frac{\partial \mathcal{L}_e}{\partial W_e} = (W_e Y + \mathbf{b}_e \mathbf{1}^T - U) Y^T = (W_e Y + \mathbf{b}_e \mathbf{1}^T) Y^T - U Y^T = 0$$

Solving for W_e we have:

$$\begin{aligned} W_e Y Y^T + \mathbf{b}_e \mathbf{1}^T Y^T - U Y^T &= 0 \\ W_e Y Y^T + \frac{1}{n_t} (U \mathbf{1} - W_e Y \mathbf{1}) \mathbf{1}^T Y^T - U Y^T &= 0 \\ W_e Y Y^T - W_e Y \frac{\mathbf{1} \mathbf{1}^T}{n_t} Y^T - U Y^T + U \frac{\mathbf{1} \mathbf{1}^T}{n_t} Y^T &= 0 \\ W_e \bar{Y} \bar{Y}^T - \bar{U} \bar{Y}^T &= 0 \\ W_e &= \bar{U} \bar{Y}^\dagger \end{aligned} \quad (14)$$

- Gradient with respect to \mathbf{b}_d

$$\frac{\partial \mathcal{L}_d}{\partial \mathbf{b}_d} = (W_d Z + \mathbf{b}_d \mathbf{1}^T - Y) \mathbf{1} = W_d Z \mathbf{1} + n_t \mathbf{b}_d - Y \mathbf{1} = 0$$

Solving for \mathbf{b}_d we have:

$$\mathbf{b}_d = \frac{1}{n_t}(Y \mathbf{1} - W_d Z \mathbf{1}) \quad (15)$$

- Gradient with respect to W_d

$$\frac{\partial \mathcal{L}_d}{\partial W_d} = (W_d Z + \mathbf{b}_d \mathbf{1}^T - Y) Z^T = W_d Z Z^T + \mathbf{b}_d \mathbf{1}^T Z^T - Y Z^T = 0$$

Solving for W_d we have:

$$\begin{aligned} W_d Z Z^T + \mathbf{b}_d \mathbf{1}^T Z^T - Y Z^T &= 0 \\ W_d Z Z^T + \frac{1}{n_t} (Y \mathbf{1} - W_d Z \mathbf{1}) \mathbf{1}^T Z^T - Y Z^T &= 0 \\ W_d Z Z^T - W_d Z \frac{\mathbf{1} \mathbf{1}^T}{n_t} Z^T - Y Z^T + Y \frac{\mathbf{1} \mathbf{1}^T}{n_t} Z^T &= 0 \\ W_d \bar{Z} \bar{Z}^T - \bar{Y} \bar{Z}^T &= 0 \\ W_d &= \bar{Y} \bar{Z}^\dagger \end{aligned} \quad (16)$$

Recall that $Z = W_e Y + \mathbf{b}_e \mathbf{1}^T$, then using the identities $\bar{\mathbf{z}} = Z \frac{\mathbf{1}}{n_t}$ and $\bar{Z} = Z - \bar{\mathbf{z}} \mathbf{1}^T$, we have

$$\begin{aligned}\bar{\mathbf{z}} &= (W_e Y + \mathbf{b}_e \mathbf{1}^T) \mathbf{1} = W_e Y \mathbf{1} + (U \mathbf{1} - W_e Y \mathbf{1}) = \bar{\mathbf{u}} \\ \bar{Z} &= W_e \bar{Y} = \bar{U} \bar{Y}^\dagger \bar{Y}\end{aligned}\tag{17}$$

Summary: From eq. (13), eq. (14), eq. (15), eq. (16), and eq. (17), the solutions for the encoder (W_e, \mathbf{b}_e) and decoder (W_d, \mathbf{b}_d) are:

$$\begin{aligned}W_e &= \bar{U} \bar{Y}^\dagger, & \mathbf{b}_e &= \frac{1}{n_t} (U \mathbf{1} - W_e Y \mathbf{1}) = \bar{\mathbf{u}} - \bar{U} \bar{Y}^\dagger \bar{\mathbf{y}} \\ W_d &= \bar{Y} \bar{Z}^\dagger = \bar{Y} (\bar{U} \bar{Y}^\dagger \bar{Y})^\dagger, & \mathbf{b}_d &= \frac{1}{n_t} (Y \mathbf{1} - W_d Z \mathbf{1}) = \bar{\mathbf{y}} - \bar{Y} (\bar{U} \bar{Y}^\dagger \bar{Y})^\dagger \bar{\mathbf{u}}\end{aligned}$$

5.2. Derivation of $W_e, \mathbf{b}_e, W_d, \mathbf{b}_d$ for nPOP

For the encoder loss, we have:

$$\mathcal{L}_e = \frac{1}{2} \|W_e U + \mathbf{b}_e \mathbf{1}^T - Y\|_F^2$$

For simplicity, let's denote $Z = W_e U + \mathbf{b}_e \mathbf{1}^T$. Then, the loss for decoder given pretrained encoder is:

$$\mathcal{L}_d = \frac{1}{2} \|W_d Z + \mathbf{b}_d \mathbf{1}^T - U\|_F^2$$

Recall that $Z = W_e U + \mathbf{b}_e \mathbf{1}^T$, then using the identities $\bar{\mathbf{z}} = Z \frac{\mathbf{1}}{n_t}$ and $\bar{Z} = Z - \bar{\mathbf{z}} \mathbf{1}^T$, we have

$$\begin{aligned}\bar{\mathbf{z}} &= \bar{\mathbf{u}} \\ \bar{Z} &= W_e \bar{U} = \bar{Y} \bar{U}^\dagger \bar{U} = G \bar{U} \bar{U}^\dagger \bar{U} = G \bar{U} = \bar{Y}\end{aligned}$$

Summary: Following the same procedure as section 5.1, we can derive the optimal solutions for the encoder (W_e, \mathbf{b}_e) and decoder (W_d, \mathbf{b}_d) for the nPOP model.

$$\begin{aligned}W_e &= \bar{Y} \bar{U}^\dagger = G \bar{U} \bar{U}^\dagger, & \mathbf{b}_e &= \frac{1}{n_t} (Y \mathbf{1} - \bar{Y} \bar{U}^\dagger U \mathbf{1}) = \bar{\mathbf{y}} - G \bar{U} \bar{U}^\dagger \bar{\mathbf{u}} = G (I - \bar{U} \bar{U}^\dagger) \bar{\mathbf{u}} \\ W_d &= \bar{U} \bar{Z}^\dagger = \bar{U} \bar{Y}^\dagger, & \mathbf{b}_d &= \frac{1}{n_t} (U \mathbf{1} - \bar{U} \bar{Z}^\dagger Z \mathbf{1}) = \bar{\mathbf{u}} - \bar{U} \bar{Y}^\dagger \bar{\mathbf{y}}\end{aligned}$$

5.3. Derivation of $W_e, \mathbf{b}_e, W_d, \mathbf{b}_d$ for mcPOP

For the encoder loss, we have:

$$\mathcal{L}_e = \frac{1}{2} \|W_e U + \mathbf{b}_e \mathbf{1}^T - Y\|_F^2$$

For simplicity, let's denote $Z = W_e U + \mathbf{b}_e \mathbf{1}^T$. Then, the loss for decoder given pretrained encoder is:

$$\mathcal{L}_d = \frac{1}{2} \|W_d Z + \mathbf{b}_d \mathbf{1}^T - U\|_F^2 + \frac{\lambda}{2} \|G^B(W_d Z + \mathbf{b}_d \mathbf{1}^T - Y)\|_F^2$$

To find the optimal values, we set all gradients to zero and solve the resulting system of equations:

- Gradient with respect to \mathbf{b}_e

$$\frac{\partial \mathcal{L}_e}{\partial \mathbf{b}_e} = (W_e U + \mathbf{b}_e \mathbf{1}^T - Y) \mathbf{1} = W_e U \mathbf{1} + n_t \mathbf{b}_e - Y \mathbf{1} = 0$$

Solving for \mathbf{b}_e we have:

$$\mathbf{b}_e = \frac{1}{n_t} (Y \mathbf{1} - W_e U \mathbf{1}) \quad (18)$$

- Gradient with respect to W_e

$$\frac{\partial \mathcal{L}_e}{\partial W_e} = (W_e U + \mathbf{b}_e \mathbf{1}^T - Y) U^T = W_e U U^T + \mathbf{b}_e \mathbf{1}^T U^T - Y U^T = 0$$

Solving for W_e we have:

$$\begin{aligned} W_e U U^T + \mathbf{b}_e \mathbf{1}^T U^T - Y U^T &= 0 \\ W_e U U^T + \frac{1}{n_t} (Y \mathbf{1} - W_e U \mathbf{1}) \mathbf{1}^T U^T - Y U^T &= 0 \\ W_e U U^T - W_e U \frac{\mathbf{1} \mathbf{1}^T}{n_t} U^T - Y U^T + Y \frac{\mathbf{1} \mathbf{1}^T}{n_t} U^T &= 0 \\ W_e \bar{U} \bar{U}^T - \bar{Y} \bar{U}^T &= 0 \\ W_e &= \bar{Y} \bar{U}^\dagger \end{aligned} \quad (19)$$

- Gradient with respect to \mathbf{b}_d

$$\frac{\partial \mathcal{L}_d}{\partial \mathbf{b}_d} = (W_d Z + \mathbf{b}_d \mathbf{1}^T - U) \mathbf{1} + \lambda G^{B^T} (G^B (W_d Z + \mathbf{b}_d \mathbf{1}^T) - Y) \mathbf{1} = 0$$

Solving for \mathbf{b}_d we have:

$$\mathbf{b}_d = \frac{1}{n_t} (U \mathbf{1} - W_d Z \mathbf{1}) - \lambda G^{B^T} (G^B (W_d Z + \mathbf{b}_d \mathbf{1}^T) - Y) \mathbf{1} \quad (20)$$

- Gradient with respect to W_d

$$\begin{aligned}\frac{\partial \mathcal{L}_d}{\partial W_d} &= (W_d Z + \mathbf{b}_d \mathbf{1}^T - U) Z^T + \lambda G^{B^T} (G^B (W_d Z + \mathbf{b}_d \mathbf{1}^T) - Y) Z^T = 0 \\ W_d Z Z^T + \mathbf{b}_d \mathbf{1}^T Z^T - U Z^T + \lambda G^{B^T} G^B W_d Z Z^T + \lambda G^{B^T} G^B \mathbf{b}_d \mathbf{1}^T Z^T - \lambda G^{B^T} Y Z^T &= 0 \\ (I + \lambda G^{B^T} G^B) W_d Z Z^T - (U Z^T + \lambda G^{B^T} Y Z^T) + (I + \lambda G^{B^T} G^B) \mathbf{b}_d \mathbf{1}^T Z^T &= 0\end{aligned}$$

Solving for W_d we have:

$$\begin{aligned}(I + \lambda G^{B^T} G^B) W_d Z Z^T &= (U Z^T + \lambda G^{B^T} Y Z^T) - (I + \lambda G^{B^T} G^B) \mathbf{b}_d \mathbf{1}^T Z^T \\ (I + \lambda G^{B^T} G^B) W_d Z Z^T &= (U Z^T + \lambda G^{B^T} Y Z^T) \\ &\quad - \frac{1}{n_t} (U \mathbf{1} - W_d Z \mathbf{1} + \lambda G^{B^T} Y \mathbf{1} - \lambda G^{B^T} G^B W_d Z \mathbf{1}) \mathbf{1}^T Z^T \\ (I + \lambda G^{B^T} G^B) W_d \bar{Z} \bar{Z}^T &= \bar{U} \bar{Z}^T + \lambda G^{B^T} \bar{Y} \bar{Z}^T \\ W_d &= (I + \lambda G^{B^T} G^B)^{-1} (\bar{U} \bar{Z}^\dagger + \lambda G^{B^T} \bar{Y} \bar{Z}^\dagger)\end{aligned}\tag{21}$$

Recall that $\bar{Z} = W_e \bar{U}$, then using the identities $\bar{\mathbf{z}} = Z \frac{\mathbf{1}}{n_t}$ and $\bar{Z} = Z - \bar{\mathbf{z}} \mathbf{1}^T$, we have

$$\begin{aligned}\bar{\mathbf{z}} &= \bar{\mathbf{u}} \\ \bar{Z} &= W_e \bar{U} = \bar{Y} \bar{U}^\dagger \bar{U} = G^B \bar{U} \bar{U}^\dagger \bar{U} = \bar{Y}\end{aligned}\tag{22}$$

Summary: From eq. (18), eq. (19), eq. (20), eq. (21), and eq. (22) we can derive the optimal solutions for the encoder (W_e , \mathbf{b}_e) and decoder (W_d , \mathbf{b}_d) for the mcPOP model.

$$\begin{aligned}W_e &= \bar{Y} \bar{U}^\dagger = G^B \bar{U} \bar{U}^\dagger, & \mathbf{b}_e &= \frac{1}{n_t} (Y \mathbf{1} - \bar{Y} \bar{U}^\dagger U \mathbf{1}) = \bar{\mathbf{y}} - G^B \bar{U} \bar{U}^\dagger \bar{\mathbf{u}}, \\ W_d &= (I + \lambda G^{B^T} G^B)^{-1} (\bar{U} \bar{Y}^\dagger + \lambda G^{B^T} \bar{Y} \bar{Y}^\dagger), \\ \mathbf{b}_d &= (I + \lambda G^{B^T} G^B)^{-1} (\bar{\mathbf{u}} + \lambda G^{B^T} \bar{\mathbf{y}} - (\bar{U} \bar{Y}^\dagger + \lambda G^{B^T} \bar{Y} \bar{Y}^\dagger) \bar{\mathbf{y}})\end{aligned}$$

5.4. Derivation of W_e , \mathbf{b}_e , W_d , \mathbf{b}_d for mcOPD

For the encoder loss, we have:

$$\mathcal{L}_e = \frac{1}{2} \|W_e Y + \mathbf{b}_e \mathbf{1}^T - U\|_F^2 + \frac{\lambda}{2} \|G^B (W_e Y + \mathbf{b}_e \mathbf{1}^T) - Y\|_F^2$$

For simplicity, let's denote $Z = W_e Y + \mathbf{b}_e \mathbf{1}^T$. Then, the loss for decoder given pretrained encoder is:

$$\mathcal{L}_d = \frac{1}{2} \|W_d Z + \mathbf{b}_d \mathbf{1}^T - G^B Z\|_F^2$$

To find the optimal values, we set all gradients to zero and solve the resulting system of equations:

- Gradient with respect to \mathbf{b}_e

$$\begin{aligned} \frac{\partial \mathcal{L}_e}{\partial \mathbf{b}_e} &= (W_e Y + \mathbf{b}_e \mathbf{1}^T - U) \mathbf{1} + \lambda G^{B^T} (G^B (W_e Y + \mathbf{b}_e \mathbf{1}^T) - Y) \mathbf{1} = 0 \\ W_e Y \mathbf{1} + \mathbf{b}_e \mathbf{1}^T \mathbf{1} - U \mathbf{1} + \lambda G^{B^T} G^B W_e Y \mathbf{1} + \lambda G^{B^T} G^B \mathbf{b}_e \mathbf{1}^T \mathbf{1} - \lambda G^{B^T} Y \mathbf{1} &= 0 \\ (I + \lambda G^{B^T} G^B) \mathbf{b}_e n_t + W_e Y \mathbf{1} - U \mathbf{1} + \lambda G^{B^T} G^B W_e Y \mathbf{1} - \lambda G^{B^T} Y \mathbf{1} &= 0 \end{aligned}$$

Solving for \mathbf{b}_e we have:

$$\mathbf{b}_e = \frac{1}{n_t} (I + \lambda G^{B^T} G^B)^{-1} (U \mathbf{1} - W_e Y \mathbf{1} - \lambda G^{B^T} G^B W_e Y \mathbf{1} + \lambda G^{B^T} Y \mathbf{1})$$

- Gradient with respect to W_e

$$\begin{aligned} \frac{\partial \mathcal{L}_e}{\partial W_e} &= (W_e Y + \mathbf{b}_e \mathbf{1}^T - U) Y^T + \lambda G^{B^T} (G^B (W_e Y + \mathbf{b}_e \mathbf{1}^T) - Y) Y^T = 0 \\ W_e Y Y^T + \mathbf{b}_e \mathbf{1}^T Y^T - U Y^T + \lambda G^{B^T} G^B W_e Y Y^T + \lambda G^{B^T} G^B \mathbf{b}_e \mathbf{1}^T Y^T - \lambda G^{B^T} Y Y^T &= 0 \\ (I + \lambda G^{B^T} G^B) W_e Y Y^T + (I + \lambda G^{B^T} G^B) \mathbf{b}_e \mathbf{1}^T Y^T - U Y^T - \lambda G^{B^T} Y Y^T &= 0 \end{aligned}$$

Solving for W_e we have:

$$\begin{aligned} (I + \lambda G^{B^T} G^B) W_e Y Y^T &= U Y^T + \lambda G^{B^T} Y Y^T \\ &\quad - \frac{1}{n_t} (U \mathbf{1} - W_e Y \mathbf{1} - \lambda G^{B^T} G^B W_e Y \mathbf{1} + \lambda G^{B^T} Y \mathbf{1}) \mathbf{1}^T Y^T \\ (I + \lambda G^{B^T} G^B) W_e \bar{Y} \bar{Y}^T &= \bar{U} \bar{Y}^T + \lambda G^{B^T} \bar{Y} \bar{Y}^T \\ W_e &= (I + \lambda G^{B^T} G^B)^{-1} (\bar{U} \bar{Y}^\dagger + \lambda G^{B^T} \bar{Y} \bar{Y}^\dagger) \end{aligned} \tag{23}$$

Substituting W_e back into \mathbf{b}_e we have:

$$\begin{aligned}
\mathbf{b}_e &= \frac{1}{n_t}(I + \lambda G^{BT} G^B)^{-1}(U\mathbf{1} - W_e Y\mathbf{1} - \lambda G^{BT} G^B W_e Y\mathbf{1} + \lambda G^{BT} Y\mathbf{1}) \\
&= \frac{1}{n_t}(I + \lambda G^{BT} G^B)^{-1}(U\mathbf{1} - (I + \lambda G^{BT} G^B) W_e Y\mathbf{1} + \lambda G^{BT} Y\mathbf{1}) \\
&= (I + \lambda G^{BT} G^B)^{-1}(U\mathbf{1} - (\bar{U}\bar{Y}^\dagger + \lambda G^{BT} \bar{Y}\bar{Y}^\dagger) Y\mathbf{1} + \lambda G^{BT} Y\mathbf{1}) \frac{1}{n_t} \\
&= (I + \lambda G^{BT} G^B)^{-1}(\bar{\mathbf{u}} + \lambda G^{BT} \bar{\mathbf{y}} - (\bar{U}\bar{Y}^\dagger + \lambda G^{BT} \bar{Y}\bar{Y}^\dagger) \bar{\mathbf{y}})
\end{aligned} \tag{24}$$

- Gradient with respect to \mathbf{b}_d

$$\frac{\partial \mathcal{L}_d}{\partial \mathbf{b}_d} = (W_d Z + \mathbf{b}_d \mathbf{1}^T - G^B Z)\mathbf{1} = W_d Z\mathbf{1} + \mathbf{b}_d \mathbf{1}^T \mathbf{1} - G^B Z\mathbf{1} = 0$$

Solving for \mathbf{b}_d we have:

$$\mathbf{b}_d = \frac{1}{n_t}(G^B Z\mathbf{1} - W_d Z\mathbf{1}) = G^B \bar{\mathbf{z}} - W_d \bar{\mathbf{z}} \tag{25}$$

- Gradient with respect to W_d

$$\frac{\partial \mathcal{L}_d}{\partial W_d} = (W_d Z + \mathbf{b}_d \mathbf{1}^T - G^B Z)Z^T = W_d Z Z^T + \mathbf{b}_d \mathbf{1}^T Z^T - G^B Z Z^T = 0$$

Solving for W_d we have:

$$\begin{aligned}
W_d Z Z^T + \mathbf{b}_d \mathbf{1}^T Z^T - G^B Z Z^T &= 0 \\
W_d \bar{Z} \bar{Z}^T &= G^B \bar{Z} \bar{Z}^T \\
W_d &= G^B \bar{Z} \bar{Z}^\dagger
\end{aligned} \tag{26}$$

- Recall that

$$\begin{aligned}
Z &= W_e Y + \mathbf{b}_e \mathbf{1}^T \\
&= (I + \lambda G^{BT} G^B)^{-1} \left((\bar{U}\bar{Y}^\dagger + \lambda G^{BT} \bar{Y}\bar{Y}^\dagger) Y + (\bar{\mathbf{u}} + \lambda G^{BT} \bar{\mathbf{y}} - (\bar{U}\bar{Y}^\dagger + \lambda G^{BT} \bar{Y}\bar{Y}^\dagger) \bar{\mathbf{y}}) \mathbf{1}^T \right) \\
&= (I + \lambda G^{BT} G^B)^{-1} \left(\bar{U}\bar{Y}^\dagger Y - \bar{U}\bar{Y}^\dagger \bar{\mathbf{y}} \mathbf{1}^T + \lambda G^{BT} \bar{Y}\bar{Y}^\dagger Y - \lambda G^{BT} \bar{Y}\bar{Y}^\dagger \bar{\mathbf{y}} \mathbf{1}^T + (\bar{\mathbf{u}} + \lambda G^{BT} \bar{\mathbf{y}}) \mathbf{1}^T \right) \\
&= (I + \lambda G^{BT} G^B)^{-1} \left(\bar{U}\bar{Y}^\dagger \bar{Y} + \lambda G^{BT} \bar{Y}\bar{Y}^\dagger \bar{Y} + (\bar{\mathbf{u}} + \lambda G^{BT} \bar{\mathbf{y}}) \mathbf{1}^T \right) \\
&= (I + \lambda G^{BT} G^B)^{-1} \left(\bar{U}\bar{Y}^\dagger \bar{Y} + \lambda G^{BT} \bar{Y} \right) + (I + \lambda G^{BT} G^B)^{-1} \left((\bar{\mathbf{u}} + \lambda G^{BT} \bar{\mathbf{y}}) \mathbf{1}^T \right)
\end{aligned}$$

then using the identities $\bar{\mathbf{z}} = Z \frac{\mathbf{1}}{n_t}$ and $\bar{Z} = Z - \bar{\mathbf{z}} \mathbf{1}^T$, we have

$$\begin{aligned}\bar{\mathbf{z}} &= (I + \lambda G^{B^T} G^B)^{-1} (\bar{\mathbf{u}} + \lambda G^{B^T} \bar{\mathbf{y}}) \\ \bar{Z} &= (I + \lambda G^{B^T} G^B)^{-1} (\bar{U} \bar{Y}^\dagger \bar{Y} + \lambda G^{B^T} \bar{Y})\end{aligned}\tag{27}$$

Summary: From eq. (24), eq. (23), eq. (25), eq. (26), and eq. (27) we can derive the optimal solutions for the encoder (W_e, \mathbf{b}_e) and decoder (W_d, \mathbf{b}_d) for the mcOPO model.

$$\begin{aligned}W_e &= (I + \lambda G^{B^T} G^B)^{-1} (\bar{U} \bar{Y}^\dagger + \lambda G^{B^T} \bar{Y} \bar{Y}^\dagger), \\ \mathbf{b}_e &= (I + \lambda G^{B^T} G^B)^{-1} (\bar{\mathbf{u}} + \lambda G^{B^T} \bar{\mathbf{y}} - (\bar{U} \bar{Y}^\dagger + \lambda G^{B^T} \bar{Y} \bar{Y}^\dagger) \bar{\mathbf{y}}) \\ W_d &= G^B \bar{Z} \bar{Z}^\dagger, \quad \mathbf{b}_d = G^B (I - \bar{Z} \bar{Z}^\dagger) \bar{\mathbf{z}}\end{aligned}$$

5.5. Derivation of $W_e, \mathbf{b}_e, W_d, \mathbf{b}_d$ for TAEN

The derivation is similar to the mcOPO in section 5.4, the key different is $U = \mathbf{u}_0 \mathbf{1}^T \implies \bar{\mathbf{u}} = \mathbf{u}_0, \bar{U} = 0$. Therefore, the optimal solutions for the encoder (W_e, \mathbf{b}_e) and decoder (W_d, \mathbf{b}_d) for the TAEN model are:

Summary: From eq. (24), eq. (23), eq. (25), eq. (26), and eq. (27) we can derive the optimal solutions for the encoder (W_e, \mathbf{b}_e) and decoder (W_d, \mathbf{b}_d) for the TAEN model.

$$\begin{aligned}W_e &= (I + \lambda G^{B^T} G^B)^{-1} (\lambda G^{B^T} \bar{Y} \bar{Y}^\dagger), \\ \mathbf{b}_e &= (I + \lambda G^{B^T} G^B)^{-1} (\mathbf{u}_0 + \lambda G^{B^T} \bar{\mathbf{y}} - \lambda G^{B^T} \bar{Y} \bar{Y}^\dagger \bar{\mathbf{y}}) \\ W_d &= G^B \bar{Z} \bar{Z}^\dagger, \quad \mathbf{b}_d = G^B (I - \bar{Z} \bar{Z}^\dagger) \bar{\mathbf{z}}\end{aligned}$$

where

$$\begin{aligned}\bar{\mathbf{z}} &= (I + \lambda G^{B^T} G^B)^{-1} (\mathbf{u}_0 + \lambda G^{B^T} \bar{\mathbf{y}}) \\ \bar{Z} &= (I + \lambda G^{B^T} G^B)^{-1} (\lambda G^{B^T} \bar{Y})\end{aligned}$$

5.6. Derivation of $W_e, \mathbf{b}_e, W_d, \mathbf{b}_d$ for nPOP - simultaneous training

We consider the optimization of the nPOP model with the encoder and decoder trained together. The combined loss function is given as:

$$\mathcal{L} = \frac{1}{2} \|W_e U + \mathbf{b}_e \mathbf{1}^T - Y\|_F^2 + \frac{\beta}{2} \|W_d (W_e U + \mathbf{b}_e \mathbf{1}^T) + \mathbf{b}_d \mathbf{1}^T - U\|_F^2$$

For simplicity, let's denote $Z = W_e U + \mathbf{b}_e \mathbf{1}^T$. Then our loss function becomes:

$$\mathcal{L} = \frac{1}{2}\|Z - Y\|_F^2 + \frac{\beta}{2}\|W_d Z + \mathbf{b}_d \mathbf{1}^T - U\|_F^2$$

To find the optimal values, we set all gradients to zero and solve the resulting system of equations:

- Gradient with respect to \mathbf{b}_d

$$\frac{\partial \mathcal{L}}{\partial \mathbf{b}_d} = (W_d Z + \mathbf{b}_d \mathbf{1}^T - U) \mathbf{1} = W_d Z \mathbf{1} + n_t \mathbf{b}_d - U \mathbf{1} = 0$$

Solving for \mathbf{b}_d we have:

$$\mathbf{b}_d = \frac{1}{n_t}(U \mathbf{1} - W_d Z \mathbf{1}) \quad (28)$$

- Gradient with respect to W_d

$$\frac{\partial \mathcal{L}}{\partial W_d} = (W_d Z + \mathbf{b}_d \mathbf{1}^T - U) Z^T = W_d Z Z^T + \mathbf{b}_d \mathbf{1}^T Z^T - U Z^T = 0$$

Solving for W_d we have:

$$\begin{aligned} W_d Z Z^T + \mathbf{b}_d \mathbf{1}^T Z^T - U Z^T &= 0 \\ W_d Z Z^T - W_d Z \frac{\mathbf{1} \mathbf{1}^T}{n_t} Z^T - U Z^T + U \frac{\mathbf{1} \mathbf{1}^T}{n_t} Z^T &= 0 \\ W_d \bar{Z} \bar{Z}^T - \bar{U} \bar{Z}^T &= 0 \\ W_d &= \bar{U} \bar{Z}^\dagger \end{aligned} \quad (29)$$

where $\bar{Z} = W_e \bar{U}$. From the condition for W_d , $W_d \bar{Z} \bar{Z}^T - \bar{U} \bar{Z}^T = W_d W_e \bar{U} \bar{U}^T W_e^T - \bar{U} \bar{U}^T W_e^T = 0$, then

$$W_e \bar{U} \bar{U}^T = W_e \bar{U} \bar{U}^T W_e^T W_d^T \quad (30)$$

we have $W_d W_e \bar{U} \bar{U}^T W_e^T W_d^T$ is symmetric, and thus $W_d W_e \bar{U} \bar{U}^T$ is also symmetric. In other words, we have a relationship,

$$W_d W_e \bar{U} \bar{U}^T = \bar{U} \bar{U}^T W_e^T W_d^T$$

From eq. (30), we have

$$W_e \bar{U} \bar{U}^T = W_e W_d W_e \bar{U} \bar{U}^T \quad (31)$$

- Gradient with respect to \mathbf{b}_e

$$\begin{aligned} \frac{\partial \mathcal{L}}{\partial \mathbf{b}_e} &= (Z - Y) \mathbf{1} + \beta [W_d^T (W_d Z + \mathbf{b}_d \mathbf{1}^T - U) \mathbf{1}] \\ &= Z \mathbf{1} - Y \mathbf{1} + \beta [W_d^T (W_d Z + \mathbf{b}_d \mathbf{1}^T - U) \mathbf{1}] = 0 \end{aligned}$$

Solving for \mathbf{b}_e we have:

$$\begin{aligned}
Z\mathbf{1} - Y\mathbf{1} + \beta [W_d^T(W_d Z + \mathbf{b}_d \mathbf{1}^T - U)\mathbf{1}] &= 0 \\
Z\mathbf{1} - Y\mathbf{1} + \beta \left[(\bar{U}\bar{Z}^\dagger)^T (\bar{U}\bar{Z}^\dagger) Z\mathbf{1} + n_t (\bar{U}\bar{Z}^\dagger)^T \frac{1}{n_t} (U\mathbf{1} - (\bar{U}\bar{Z}^\dagger) Z\mathbf{1}) - (\bar{U}\bar{Z}^\dagger)^T U\mathbf{1} \right] &= 0 \\
Z\mathbf{1} - Y\mathbf{1} + \beta \left[(\bar{U}\bar{Z}^\dagger)^T (\bar{U}\bar{Z}^\dagger) Z\mathbf{1} + (\bar{U}\bar{Z}^\dagger)^T (U\mathbf{1} - (\bar{U}\bar{Z}^\dagger) Z\mathbf{1}) - (\bar{U}\bar{Z}^\dagger)^T U\mathbf{1} \right] &= 0 \\
Z\mathbf{1} - Y\mathbf{1} + \beta \left[\cancel{(\bar{U}\bar{Z}^\dagger)^T (\bar{U}\bar{Z}^\dagger) Z\mathbf{1}} + \cancel{(\bar{U}\bar{Z}^\dagger)^T U\mathbf{1}} - \cancel{(\bar{U}\bar{Z}^\dagger)^T (\bar{U}\bar{Z}^\dagger) Z\mathbf{1}} - \cancel{(\bar{U}\bar{Z}^\dagger)^T U\mathbf{1}} \right] &= 0 \\
Z\mathbf{1} - Y\mathbf{1} &= 0 \\
W_e U\mathbf{1} + \mathbf{b}_e \mathbf{1}^T \mathbf{1} - Y\mathbf{1} &= 0 \\
\mathbf{b}_e &= \frac{1}{n_t} (Y\mathbf{1} - W_e U\mathbf{1})
\end{aligned} \tag{32}$$

- Gradient with respect to W_e

$$\begin{aligned}
\frac{\partial \mathcal{L}}{\partial W_e} &= (Z - Y)U^T + \beta [W_d^T(W_d Z + \mathbf{b}_d \mathbf{1}^T - U)U^T] \\
&= ZU^T - YU^T + \beta [W_d^T(W_d ZU^T + \mathbf{b}_d \mathbf{1}^T U^T - UU^T)] = 0
\end{aligned}$$

We first simplify the equation:

$$\begin{aligned}
ZU^T - YU^T + \beta [W_d^T(W_d ZU^T + \mathbf{b}_d \mathbf{1}^T U^T - UU^T)] &= 0 \\
W_e \bar{U}\bar{U}^T - \bar{Y}\bar{U}^T + \beta \left[W_d^T W_d ZU^T + W_d^T \frac{1}{n_t} (U\mathbf{1} - W_d Z\mathbf{1})\mathbf{1}^T U^T - W_d^T UU^T \right] &= 0 \\
W_e \bar{U}\bar{U}^T - \bar{Y}\bar{U}^T + \beta [W_d^T W_d \bar{Z}\bar{U}^T - W_d^T \bar{U}\bar{U}^T] &= 0 \\
W_e \bar{U}\bar{U}^T - \bar{Y}\bar{U}^T + \beta [W_d^T W_d W_e \bar{U}\bar{U}^T - W_d^T \bar{U}\bar{U}^T] &= 0
\end{aligned}$$

The best we can solve for W_e is

$$\begin{aligned}
(I + \beta W_d^T W_d) W_e \bar{U}\bar{U}^T &= \bar{Y}\bar{U}^T + \beta W_d^T \bar{U}\bar{U}^T \\
W_e &= (I + \beta W_d^T W_d)^{-1} (\bar{Y}\bar{U}^T + \beta W_d^T \bar{U}\bar{U}^T) (\bar{U}\bar{U}^T)^\dagger \\
&\text{since } A^T (AA^T)^\dagger = A^\dagger, \text{ so} \\
W_e &= (I + \beta W_d^T W_d)^{-1} (G^B \bar{U}\bar{U}^\dagger + \beta W_d^T \bar{U}\bar{U}^\dagger).
\end{aligned} \tag{33}$$

Summary: From eq. (28), eq. (29), eq. (32), eq. (33), and eq. (31), we can derive the optimal solutions for the encoder (W_e, \mathbf{b}_e) and decoder (W_d, \mathbf{b}_d) for nOPO model as training autoencoder simultaneously.

$$\begin{aligned} W_e &= (I + \beta W_d^T W_d)^{-1} (G^B \bar{U} \bar{U}^\dagger + \beta W_d^T \bar{U} \bar{U}^\dagger), & \mathbf{b}_e &= \bar{\mathbf{y}} - W_e \bar{\mathbf{u}}, \\ W_d &= \bar{U} (W_e \bar{U})^\dagger, & \mathbf{b}_d &= \bar{\mathbf{u}} - W_d \bar{\mathbf{y}}, \\ W_e \bar{U} \bar{U}^T &= W_e W_d W_e \bar{U} \bar{U}^T \end{aligned}$$

5.7. Derivation of $W_e, \mathbf{b}_e, W_d, \mathbf{b}_d$ for nOPO - simultaneous training

We consider the optimization of the nOPO model with the encoder and decoder trained together. The combined loss function is given as:

$$\mathcal{L} = \frac{1}{2} \|W_e Y + \mathbf{b}_e \mathbf{1}^T - U\|_F^2 + \frac{\beta}{2} \|W_d(W_e Y + \mathbf{b}_e \mathbf{1}^T) + \mathbf{b}_d \mathbf{1}^T - Y\|_F^2$$

For simplicity, let's denote $Z = W_e Y + \mathbf{b}_e \mathbf{1}^T$. Then our loss function becomes:

$$\mathcal{L} = \frac{1}{2} \|Z - U\|_F^2 + \frac{\beta}{2} \|W_d Z + \mathbf{b}_d \mathbf{1}^T - Y\|_F^2$$

To find the optimal values, we set all gradients to zero and solve the resulting system of equations:

- Gradient with respect to \mathbf{b}_d

$$\frac{\partial \mathcal{L}}{\partial \mathbf{b}_d} = (W_d Z + \mathbf{b}_d \mathbf{1}^T - Y) \mathbf{1} = W_d Z \mathbf{1} + n_t \mathbf{b}_d - Y \mathbf{1} = 0$$

Solving for \mathbf{b}_d we have:

$$\mathbf{b}_d = \frac{1}{n_t} (Y \mathbf{1} - W_d Z \mathbf{1}) \quad (34)$$

- Gradient with respect to W_d

$$\frac{\partial \mathcal{L}}{\partial W_d} = (W_d Z + \mathbf{b}_d \mathbf{1}^T - Y) Z^T = W_d Z Z^T + \mathbf{b}_d \mathbf{1}^T Z^T - Y Z^T = 0$$

Solving for W_d we have:

$$\begin{aligned} W_d Z Z^T + \mathbf{b}_d \mathbf{1}^T Z^T - Y Z^T &= 0 \\ W_d Z Z^T - W_d Z \frac{\mathbf{1} \mathbf{1}^T}{n_t} Z^T - Y Z^T + Y \frac{\mathbf{1} \mathbf{1}^T}{n_t} Z^T &= 0 \\ W_d \bar{Z} \bar{Z}^T - \bar{Y} \bar{Z}^T &= 0 \\ W_d &= \bar{Y} \bar{Z}^\dagger \end{aligned} \quad (35)$$

where $\bar{Z} = W_e \bar{Y}$. Form the condition for W_d , $W_d \bar{Z} \bar{Z}^T - \bar{Y} \bar{Z}^T = W_d W_e \bar{Y} \bar{Y}^T W_e^T - \bar{Y} \bar{Y}^T W_e^T = 0$, then

$$W_e \bar{Y} \bar{Y}^T = W_e \bar{Y} \bar{Y}^T W_e^T W_d^T \quad (36)$$

we have $W_d W_e \bar{Y} \bar{Y}^T W_e^T W_d^T$ is symmetric, and thus $W_d W_e \bar{Y} \bar{Y}^T$ is also symmetric. In other words, we have a relationship,

$$W_d W_e \bar{Y} \bar{Y}^T = \bar{Y} \bar{Y}^T W_e^T W_d^T$$

From eq. (36), we have

$$W_e \bar{Y} \bar{Y}^T = W_e W_d W_e \bar{Y} \bar{Y}^T \quad (37)$$

- Gradient with respect to \mathbf{b}_e

$$\begin{aligned} \frac{\partial \mathcal{L}}{\partial \mathbf{b}_e} &= (Z - U)\mathbf{1} + \beta W_d^T (W_d Z + \mathbf{b}_d \mathbf{1}^T - Y)\mathbf{1} \\ &= Z\mathbf{1} - U\mathbf{1} + \beta W_d^T (W_d Z + \mathbf{b}_d \mathbf{1}^T - Y)\mathbf{1} = 0 \end{aligned}$$

Solving for \mathbf{b}_e we have:

$$\begin{aligned} Z\mathbf{1} - U\mathbf{1} + \beta [W_d^T (W_d Z + \mathbf{b}_d \mathbf{1}^T - Y)\mathbf{1}] &= 0 \\ Z\mathbf{1} - U\mathbf{1} + \beta \left[(\bar{Y} \bar{Z}^\dagger)^T (\bar{Y} \bar{Z}^\dagger) Z\mathbf{1} + n_t (\bar{Y} \bar{Z}^\dagger)^T \frac{1}{n_t} (Y\mathbf{1} - (\bar{Y} \bar{Z}^\dagger) Z\mathbf{1}) - (\bar{Y} \bar{Z}^\dagger)^T Y\mathbf{1} \right] &= 0 \\ Z\mathbf{1} - U\mathbf{1} + \beta \left[(\bar{Y} \bar{Z}^\dagger)^T (\bar{Y} \bar{Z}^\dagger) Z\mathbf{1} + (\bar{Y} \bar{Z}^\dagger)^T (Y\mathbf{1} - (\bar{Y} \bar{Z}^\dagger) Z\mathbf{1}) - (\bar{Y} \bar{Z}^\dagger)^T Y\mathbf{1} \right] &= 0 \\ Z\mathbf{1} - U\mathbf{1} + \beta \left[\cancel{(\bar{Y} \bar{Z}^\dagger)^T (\bar{Y} \bar{Z}^\dagger) Z\mathbf{1}} + \cancel{(\bar{Y} \bar{Z}^\dagger)^T Y\mathbf{1}} - \cancel{(\bar{Y} \bar{Z}^\dagger)^T (\bar{Y} \bar{Z}^\dagger) Z\mathbf{1}} - \cancel{(\bar{Y} \bar{Z}^\dagger)^T Y\mathbf{1}} \right] &= 0 \\ Z\mathbf{1} - U\mathbf{1} &= 0 \\ W_e Y\mathbf{1} + \mathbf{b}_e \mathbf{1}^T \mathbf{1} - U\mathbf{1} &= 0 \\ \mathbf{b}_e &= \frac{1}{n_t} (U\mathbf{1} - W_e Y\mathbf{1}) \end{aligned} \quad (38)$$

- Gradient with respect to W_e

$$\begin{aligned} \frac{\partial \mathcal{L}}{\partial W_e} &= (Z - U)Y^T + \beta W_d^T (W_d Z + \mathbf{b}_d \mathbf{1}^T - Y)Y^T \\ &= ZY^T - UY^T + \beta W_d^T (W_d ZY^T + \mathbf{b}_d \mathbf{1}^T Y^T - YY^T) = 0 \end{aligned}$$

We first simplify the equation:

$$\begin{aligned}
ZY^T - UY^T + \beta W_d^T (W_d ZY^T + \mathbf{b}_d \mathbf{1}^T Y^T - YY^T) &= 0 \\
W_e \bar{Y} \bar{Y}^T - \bar{U} \bar{Y}^T + \beta \left[W_d^T W_d ZY^T + W_d^T \frac{1}{n_t} (Y \mathbf{1} - W_d Z \mathbf{1}) \mathbf{1}^T Y^T - W_d^T YY^T \right] &= 0 \\
W_e \bar{Y} \bar{Y}^T - \bar{U} \bar{Y}^T + \beta [W_d^T W_d \bar{Z} \bar{Y}^T - W_d^T \bar{Y} \bar{Y}^T] &= 0 \\
W_e \bar{Y} \bar{Y}^T - \bar{U} \bar{Y}^T + \beta [W_d^T W_d W_e \bar{Y} \bar{Y}^T - W_d^T \bar{Y} \bar{Y}^T] &= 0
\end{aligned}$$

The best we can solve for W_e is

$$\begin{aligned}
(I + W_d^T \beta W_d) W_e \bar{Y} \bar{Y}^T &= \bar{U} \bar{Y}^T + \beta W_d^T \bar{Y} \bar{Y}^T \\
W_e &= (I + \beta W_d^T W_d)^{-1} (\bar{U} \bar{Y}^T + \beta W_d^T \bar{Y} \bar{Y}^T) (\bar{Y} \bar{Y}^T)^\dagger \\
&\text{since } A^T (AA^T)^\dagger = A^\dagger, \text{ so} \\
W_e &= (I + \beta W_d^T W_d)^{-1} (\bar{U} \bar{Y}^\dagger + \beta W_d^T \bar{Y} \bar{Y}^\dagger).
\end{aligned} \tag{39}$$

Summary: From eq. (34), eq. (35), eq. (38), eq. (39), and eq. (37), we can derive the optimal solutions for the encoder (W_e , \mathbf{b}_e) and decoder (W_d , \mathbf{b}_d) for nPO model as training autoencoder simultaneously.

$$\begin{aligned}
W_e &= (I + \beta W_d^T W_d)^{-1} (\bar{U} \bar{Y}^\dagger + \beta W_d^T \bar{Y} \bar{Y}^\dagger), & \mathbf{b}_e &= \bar{\mathbf{u}} - W_e \bar{\mathbf{y}}, \\
W_d &= \bar{Y} (W_e \bar{Y})^\dagger, & \mathbf{b}_d &= \bar{\mathbf{y}} - W_d \bar{\mathbf{u}}, \\
W_e \bar{Y} \bar{Y}^T &= W_e W_d W_e \bar{Y} \bar{Y}^T
\end{aligned}$$

References

- [1] Hemant K Aggarwal, Merry P Mani, and Mathews Jacob. Modl: Model-based deep learning architecture for inverse problems. *IEEE transactions on medical imaging*, 38(2):394–405, 2018.
- [2] Manal Almaeen, Yasir Alanazi, Nobuo Sato, W Melnitchouk, Michelle P Kuchera, and Yaohang Li. Variational autoencoder inverse mapper: An end-to-end deep learning framework for inverse problems. In *2021 International Joint Conference on Neural Networks (IJCNN)*, pages 1–8. IEEE, 2021.
- [3] Simon Arridge, Peter Maass, Ozan Öktem, and Carola-Bibiane Schönlieb. Solving inverse problems using data-driven models. *Acta Numerica*, 28:1–174, 2019.
- [4] Mark Austin, Parastoo Delgoshaei, Maria Coelho, and Mohammad Heidarnejad. Architecting smart city digital twins: Combined semantic model and machine learning approach. *Journal of Management in Engineering*, 36(4):04020026, 2020.
- [5] Shivam Barwey and Romit Maulik. Interpretable fine-tuning for graph neural network surrogate models. *arXiv preprint arXiv:2311.07548*, 2023.
- [6] Jens Berg and Kaj Nyström. Neural network augmented inverse problems for pdes. *arXiv preprint arXiv:1712.09685*, 2017.
- [7] Chris M Bishop. Training with noise is equivalent to tikhonov regularization. *Neural computation*, 7(1):108–116, 1995.
- [8] Yoeri E Boink and Christoph Brune. Learned svd: solving inverse problems via hybrid autoencoding. *arXiv preprint arXiv:1912.10840*, 2019.

- [9] James Bradbury, Roy Frostig, Peter Hawkins, Matthew James Johnson, Chris Leary, Dougal Maclaurin, George Necula, Adam Paszke, Jake VanderPlas, Skye Wanderman-Milne, and Qiao Zhang. JAX: composable transformations of Python+NumPy programs, 2018.
- [10] Tan Bui-Thanh and Omar Ghattas. Analysis of the Hessian for inverse scattering problems. Part I: Inverse shape scattering of acoustic waves. *Inverse Problems*, 28(5):055001, 2012. <http://users.ices.utexas.edu/%7Etanbui/PublishedPapers/CompactI.pdf>.
- [11] Tan Bui-Thanh and Omar Ghattas. Analysis of the Hessian for inverse scattering problems. Part II: Inverse medium scattering of acoustic waves. *Inverse Problems*, 28(5):055002, 2012. <http://users.ices.utexas.edu/%7Etanbui/PublishedPapers/CompactII.pdf>.
- [12] Tan Bui-Thanh and Omar Ghattas. Analysis of the Hessian for inverse scattering problems. Part III: Inverse medium scattering of electromagnetic waves. *Inverse Problems and Imaging*, 2013. <http://users.ices.utexas.edu/%7Etanbui/PublishedPapers/EM3Dmedium.pdf>.
- [13] Shengze Cai, Zhicheng Wang, Sifan Wang, Paris Perdikaris, and George Em Karniadakis. Physics-informed neural networks for heat transfer problems. *Journal of Heat Transfer*, 143(6):060801, 2021.
- [14] Min Chen, Xiaobo Shi, Yin Zhang, Di Wu, and Mohsen Guizani. Deep feature learning for medical image analysis with convolutional autoencoder neural network. *IEEE Transactions on Big Data*, 7(4):750–758, 2017.
- [15] Nan-Chen Chen, Margaret Drouhard, Rafal Kocielnik, Jina Suh, and Cecilia R Aragon. Using machine learning to support qualitative coding in social science: Shifting the focus to ambiguity. *ACM Transactions on Interactive Intelligent Systems (TiiS)*, 8(2):1–20, 2018.
- [16] Ricky TQ Chen, Yulia Rubanova, Jesse Bettencourt, and David K Duvenaud. Neural ordinary differential equations. *Advances in neural information processing systems*, 31, 2018.
- [17] Yuyao Chen, Lu Lu, George Em Karniadakis, and Luca Dal Negro. Physics-informed neural networks for inverse problems in nano-optics and metamaterials. *Optics express*, 28(8):11618–11633, 2020.
- [18] Matthias Chung, Emma Hart, Julianne Chung, Bas Peters, and Eldad Haber. Paired autoencoders for inverse problems. *arXiv preprint arXiv:2405.13220*, 2024.
- [19] Paul G Constantine, Carson Kent, and Tan Bui-Thanh. Accelerating markov chain monte carlo with active subspaces. *SIAM Journal on Scientific Computing*, 38(5):A2779–A2805, 2016.
- [20] Salvatore Cuomo, Vincenzo Schiano Di Cola, Fabio Giampaolo, Gianluigi Rozza, Maziar Raissi, and Francesco Piccialli. Scientific machine learning through physics-informed neural networks: Where we are and what’s next. *Journal of Scientific Computing*, 92(3):88, 2022.
- [21] Jia Deng, Wei Dong, Richard Socher, Li-Jia Li, Kai Li, and Li Fei-Fei. Imagenet: A large-scale hierarchical image database. In *2009 IEEE conference on computer vision and pattern recognition*, pages 248–255. Ieee, 2009.
- [22] Harris Drucker and Yann Le Cun. Improving generalization performance using double backpropagation. *IEEE transactions on neural networks*, 3(6):991–997, 1992.
- [23] Robert Eymard, Thierry Gallouët, and Raphaële Herbin. Finite volume methods. *Handbook of numerical analysis*, 7:713–1018, 2000.
- [24] Tiffany Fan, Kailai Xu, Jay Pathak, and Eric Darve. Solving inverse problems in steady-state navier-stokes equations using deep neural networks. *arXiv preprint arXiv:2008.13074*, 2020.
- [25] Xinlong Feng and Zhinan Zhang. The rank of a random matrix. *Applied Mathematics and Computation*, 185(1):689–694, 2007.
- [26] Chris Finlay and Adam M Oberman. Scaleable input gradient regularization for adversarial robustness. *Machine Learning with Applications*, 3:100017, 2021.
- [27] Ken-ichi Funahashi and Yuichi Nakamura. Approximation of dynamical systems by continuous time recurrent neural networks. *Neural networks*, 6(6):801–806, 1993.
- [28] Nicholas Geneva and Nicholas Zabaras. Transformers for modeling physical systems. *Neural Networks*, 146:272–289, 2022.
- [29] Sergei K Godunov and I Bohachevsky. Finite difference method for numerical computation of discontinuous solutions of the equations of fluid dynamics. *Matematičeskij sbornik*, 47(3):271–306, 1959.
- [30] Hwan Goh, Sheroze Sherifdeen, Jonathan Wittmer, and Tan Bui-Thanh. Solving bayesian inverse

- problems via variational autoencoders. *arXiv preprint arXiv:1912.04212*, 2019.
- [31] Gene H Golub, Per Christian Hansen, and Dianne P O’Leary. Tikhonov regularization and total least squares. *SIAM journal on matrix analysis and applications*, 21(1):185–194, 1999.
- [32] Lovedeep Gondara. Medical image denoising using convolutional denoising autoencoders. In *2016 IEEE 16th international conference on data mining workshops (ICDMW)*, pages 241–246. IEEE, 2016.
- [33] Francisco J Gonzalez and Maciej Balajewicz. Deep convolutional recurrent autoencoders for learning low-dimensional feature dynamics of fluid systems. *arXiv preprint arXiv:1808.01346*, 2018.
- [34] Ronald B Guenther and John W Lee. *Partial differential equations of mathematical physics and integral equations*. Courier Corporation, 1996.
- [35] Kaiming He, Xinlei Chen, Saining Xie, Yanghao Li, Piotr Dollár, and Ross Girshick. Masked autoencoders are scalable vision learners. In *Proceedings of the IEEE/CVF conference on computer vision and pattern recognition*, pages 16000–16009, 2022.
- [36] Kazufumi Ito and Bangti Jin. *Inverse problems: Tikhonov theory and algorithms*, volume 22. World Scientific, 2014.
- [37] Ameya D Jagtap, Ehsan Kharazmi, and George Em Karniadakis. Conservative physics-informed neural networks on discrete domains for conservation laws: Applications to forward and inverse problems. *Computer Methods in Applied Mechanics and Engineering*, 365:113028, 2020.
- [38] Ameya D Jagtap, Zhiping Mao, Nikolaus Adams, and George Em Karniadakis. Physics-informed neural networks for inverse problems in supersonic flows. *Journal of Computational Physics*, 466:111402, 2022.
- [39] Yuchen Jin, Qiuyang Shen, Xuqing Wu, Jiefu Chen, and Yueqin Huang. A physics-driven deep-learning network for solving nonlinear inverse problems. *Petrophysics*, 61(01):86–98, 2020.
- [40] Zhaoyang Larry Jin, Yimin Liu, and Louis J Durlofsky. Deep-learning-based surrogate model for reservoir simulation with time-varying well controls. *Journal of Petroleum Science and Engineering*, 192:107273, 2020.
- [41] Jari Kaipio and Erkki Somersalo. *Statistical and computational inverse problems*, volume 160. Springer Science & Business Media, 2006.
- [42] Diederik P Kingma and Jimmy Ba. Adam: A method for stochastic optimization. *arXiv preprint arXiv:1412.6980*, 2014.
- [43] Alex Krizhevsky, Ilya Sutskever, and Geoffrey E Hinton. Imagenet classification with deep convolutional neural networks. *Advances in neural information processing systems*, 25, 2012.
- [44] Chao-Chee Ku and Kwang Y Lee. Diagonal recurrent neural networks for dynamic systems control. *IEEE transactions on neural networks*, 6(1):144–156, 1995.
- [45] Kookjin Lee and Kevin T Carlberg. Model reduction of dynamical systems on nonlinear manifolds using deep convolutional autoencoders. *Journal of Computational Physics*, 404:108973, 2020.
- [46] Randall J LeVeque. *Finite volume methods for hyperbolic problems*, volume 31. Cambridge university press, 2002.
- [47] Housen Li, Johannes Schwab, Stephan Antholzer, and Markus Haltmeier. Nett: Solving inverse problems with deep neural networks. *Inverse Problems*, 36(6):065005, 2020.
- [48] Zijie Li, Kazem Meidani, and Amir Barati Farimani. Transformer for partial differential equations’ operator learning. *arXiv preprint arXiv:2205.13671*, 2022.
- [49] Zongyi Li, Nikola Kovachki, Kamyar Azizzadenesheli, Burigede Liu, Kaushik Bhattacharya, Andrew Stuart, and Anima Anandkumar. Fourier neural operator for parametric partial differential equations. *arXiv preprint arXiv:2010.08895*, 2020.
- [50] Zongyi Li, Nikola Kovachki, Kamyar Azizzadenesheli, Burigede Liu, Kaushik Bhattacharya, Andrew Stuart, and Anima Anandkumar. Fourier neural operator for parametric partial differential equations, 2020.
- [51] Dianjing Liu, Yixuan Tan, Erfan Khoram, and Zongfu Yu. Training deep neural networks for the inverse design of nanophotonic structures. *Acs Photonics*, 5(4):1365–1369, 2018.
- [52] Lu Lu, Pengzhan Jin, Guofei Pang, Zhongqiang Zhang, and George Em Karniadakis. Learning nonlinear operators via deeponet based on the universal approximation theorem of operators. *Nature machine intelligence*, 3(3):218–229, 2021.

- [53] Sebastian Lunz, Ozan Öktem, and Carola-Bibiane Schönlieb. Adversarial regularizers in inverse problems. *Advances in neural information processing systems*, 31, 2018.
- [54] Kiyotoshi Matsuoka. Noise injection into inputs in back-propagation learning. *IEEE Transactions on Systems, Man, and Cybernetics*, 22(3):436–440, 1992.
- [55] Nima Mohajerin and Steven L Waslander. Multistep prediction of dynamic systems with recurrent neural networks. *IEEE transactions on neural networks and learning systems*, 30(11):3370–3383, 2019.
- [56] Beatriz Moya, Alberto Badías, Icíar Alfaro, Francisco Chinesta, and Elías Cueto. Digital twins that learn and correct themselves. *International Journal for Numerical Methods in Engineering*, 123(13):3034–3044, 2022.
- [57] Hai Nguyen, Jonathan Wittmer, and Tan Bui-Thanh. Dias: a data-informed active subspace regularization framework for inverse problems. *Computation*, 10(3):38, 2022.
- [58] Hai V Nguyen and Tan Bui-Thanh. A model-constrained tangent slope learning approach for dynamical systems. *International Journal of Computational Fluid Dynamics*, 36(7):655–685, 2022.
- [59] Hai V Nguyen and Tan Bui-Thanh. Tnet: A model-constrained tikhonov network approach for inverse problems. *SIAM Journal on Scientific Computing*, 46(1):C77–C100, 2024.
- [60] Jorge Nocedal and Stephen J Wright. *Numerical optimization*. Springer, 1999.
- [61] Thomas O’Leary-Roseberry, Peng Chen, Umberto Villa, and Omar Ghattas. Derivative-informed neural operator: an efficient framework for high-dimensional parametric derivative learning. *Journal of Computational Physics*, 496:112555, 2024.
- [62] Gregory Ongie, Ajil Jalal, Christopher A Metzler, Richard G Baraniuk, Alexandros G Dimakis, and Rebecca Willett. Deep learning techniques for inverse problems in imaging. *IEEE Journal on Selected Areas in Information Theory*, 1(1):39–56, 2020.
- [63] M Necati Özişik, Helcio RB Orlando, Marcelo J Colaço, and Renato M Cotta. *Finite difference methods in heat transfer*. CRC press, 2017.
- [64] Thomas O’Leary-Roseberry, Umberto Villa, Peng Chen, and Omar Ghattas. Derivative-informed projected neural networks for high-dimensional parametric maps governed by pdes. *Computer Methods in Applied Mechanics and Engineering*, 388:114199, 2022.
- [65] Samira Pakravan, Pouria A Mistani, Miguel A Aragon-Calvo, and Frederic Gibou. Solving inverse-pde problems with physics-aware neural networks. *Journal of Computational Physics*, 440:110414, 2021.
- [66] Shaowu Pan and Karthik Duraisamy. Long-time predictive modeling of nonlinear dynamical systems using neural networks. *Complexity*, 2018, 2018.
- [67] Robert L Parker. *Geophysical inverse theory*, volume 1. Princeton university press, 1994.
- [68] Nicholas Perrone and Robert Kao. A general finite difference method for arbitrary meshes. *Computers & Structures*, 5(1):45–57, 1975.
- [69] Federico Pichi, Beatriz Moya, and Jan S Hesthaven. A graph convolutional autoencoder approach to model order reduction for parametrized pdes. *Journal of Computational Physics*, 501:112762, 2024.
- [70] Tomaso Poggio and Federico Girosi. Networks for approximation and learning. *Proceedings of the IEEE*, 78(9):1481–1497, 1990.
- [71] Maziar Raissi, Paris Perdikaris, and George E Karniadakis. Physics-informed neural networks: A deep learning framework for solving forward and inverse problems involving nonlinear partial differential equations. *Journal of Computational Physics*, 378:686–707, 2019.
- [72] Singiresu S Rao. *The finite element method in engineering*. Elsevier, 2010.
- [73] M Mazhar Rathore, Syed Attique Shah, Dharendra Shukla, Elmahdi Bentafat, and Spiridon Bakiras. The role of ai, machine learning, and big data in digital twinning: A systematic literature review, challenges, and opportunities. *IEEE Access*, 9:32030–32052, 2021.
- [74] JN Reddy. An introduction to the finite element method, 1993.
- [75] Russell Reed, Seho Oh, RJ Marks, et al. Regularization using jittered training data. In *International Joint Conference on Neural Networks*, volume 3, pages 147–152, 1992.
- [76] Yaniv Romano, Michael Elad, and Peyman Milanfar. The little engine that could: Regularization by denoising (red). *SIAM Journal on Imaging Sciences*, 10(4):1804–1844, 2017.
- [77] Andrew Ross and Finale Doshi-Velez. Improving the adversarial robustness and interpretability of

- deep neural networks by regularizing their input gradients. In *Proceedings of the AAAI conference on artificial intelligence*, volume 32, 2018.
- [78] Alvaro Sanchez-Gonzalez, Jonathan Godwin, Tobias Pfaff, Rex Ying, Jure Leskovec, and Peter Battaglia. Learning to simulate complex physics with graph networks. In *International Conference on Machine Learning*, pages 8459–8468. PMLR, 2020.
- [79] Anand Pratap Singh, Shivaaji Medida, and Karthik Duraisamy. Machine-learning-augmented predictive modeling of turbulent separated flows over airfoils. *AIAA journal*, 55(7):2215–2227, 2017.
- [80] Vincent Sitzmann, Julien Martel, Alexander Bergman, David Lindell, and Gordon Wetzstein. Implicit neural representations with periodic activation functions. *Advances in neural information processing systems*, 33:7462–7473, 2020.
- [81] Arnold Sommerfeld. *Partial differential equations in physics*. Academic press, 1949.
- [82] Jian Sun, Kristopher Innanen, Tianze Zhang, and Daniel Trad. Implicit seismic full waveform inversion with deep neural representation. *Journal of Geophysical Research: Solid Earth*, 128(3):e2022JB025964, 2023.
- [83] Albert Tarantola. *Inverse problem theory and methods for model parameter estimation*. SIAM, 2005.
- [84] Hai Van Nguyen, Jau-Uei Chen, William Cole Nockolds, Wesley Lao, and Tan Bui-Thanh. A model-constrained discontinuous galerkin network (dgnnet) for compressible euler equations with out-of-distribution generalization. *arXiv preprint arXiv:2409.18371*, 2024.
- [85] A Vaswani. Attention is all you need. *Advances in Neural Information Processing Systems*, 2017.
- [86] Roman Vershynin. *High-Dimensional Probability: An Introduction with Applications in Data Science*. Cambridge Series in Statistical and Probabilistic Mathematics. Cambridge University Press, 2018.
- [87] Curtis R Vogel. *Computational methods for inverse problems*. SIAM, 2002.
- [88] Zhong Yi Wan, Leonardo Zepeda-Nunez, Anudhyan Boral, and Fei Sha. Evolve smoothly, fit consistently: Learning smooth latent dynamics for advection-dominated systems. *arXiv preprint arXiv:2301.10391*, 2023.
- [89] Sifan Wang, Hanwen Wang, and Paris Perdikaris. Learning the solution operator of parametric partial differential equations with physics-informed deepnets. *Science advances*, 7(40):eabi8605, 2021.
- [90] Yi-Jen Wang and Chin-Teng Lin. Runge-kutta neural network for identification of dynamical systems in high accuracy. *IEEE Transactions on Neural Networks*, 9(2):294–307, 1998.
- [91] Yue Wu and Youzuo Lin. Inversionnet: A real-time and accurate full waveform inversion with cnns and continuous crfs. *arXiv preprint arXiv:1811.07875*, 2018.
- [92] Yiheng Xie, Towaki Takikawa, Shunsuke Saito, Or Litany, Shiqin Yan, Numair Khan, Federico Tombari, James Tompkin, Vincent Sitzmann, and Srinath Sridhar. Neural fields in visual computing and beyond. In *Computer Graphics Forum*, volume 41, pages 641–676. Wiley Online Library, 2022.
- [93] Jiayang Xu and Karthik Duraisamy. Multi-level convolutional autoencoder networks for parametric prediction of spatio-temporal dynamics. *Computer Methods in Applied Mechanics and Engineering*, 372:113379, 2020.
- [94] Jeremy Yu, Lu Lu, Xuhui Meng, and George Em Karniadakis. Gradient-enhanced physics-informed neural networks for forward and inverse pde problems. *Computer Methods in Applied Mechanics and Engineering*, 393:114823, 2022.
- [95] Kai Zhang, Wangmeng Zuo, Shuhang Gu, and Lei Zhang. Learning deep cnn denoiser prior for image restoration. In *Proceedings of the IEEE conference on computer vision and pattern recognition*, pages 3929–3938, 2017.
- [96] Michael S Zhdanov. *Geophysical inverse theory and regularization problems*, volume 36. Elsevier, 2002.
- [97] Qinyu Zhuang, Juan Manuel Lorenzi, Hans-Joachim Bungartz, and Dirk Hartmann. Model order reduction based on runge–kutta neural networks. *Data-Centric Engineering*, 2, 2021.